The Planetary Science Journal, 5:84 (26pp), 2024 April https://doi.org/10.3847/PSJ/ad2933

Rotational Study of 5:3 and 7:4 Resonant Objects within the Main Classical Trans-Neptunian Belt

Audrey Thirouin[1] and Scott S. Sheppard[2]
[1] Lowell Observatory, 1400 West Mars Hill Road, Flagstaff, AZ 86001, USA; thirouin@lowell.edu
[2] Earth and Planets Laboratory, Carnegie Institution for Science, 5241 Broad Branch Road NW, Washington, DC 20015, USA

Received 2023 October 3; revised 2024 February 6; accepted 2024 February 7; published 2024 April 1

Abstract

The 5:3 and 7:4 mean motion resonances of Neptune are at 42.3 and 43.7 au, respectively, and overlap with objects in the classical trans-Neptunian belt (Kuiper Belt). We report the complete/partial lightcurves of 13 and 14 trans-Neptunian objects (TNOs) in the 5:3 and 7:4 resonances, respectively. We report a most likely contact binary in the 7:4 resonance, 2013 FR$_{28}$, with a periodicity of 13.97 ± 0.04 hr and a lightcurve amplitude of 0.94 ± 0.02 mag. With a V-/U-shaped lightcurve, 2013 FR$_{28}$ has one of the largest well-sampled TNO amplitudes observed with ground-based observations, comparable to the well-determined contact binary 2001 QG$_{298}$. 2013 FR$_{28}$ has a mass ratio $q \sim 1$ with a density $\rho \sim 1$ g cm^{-3}. We find several objects with large amplitudes and classify 2004 SC$_{60}$, 2006 CJ$_{69}$, and 2013 BN$_{82}$ as likely contact binaries and 2001 QF$_{331}$, 2003 YW$_{179}$, and 2015 FP$_{345}$ as likely elongated objects. We observe the 17:9 resonant or classical object 2003 SP$_{317}$ that we classify as a likely contact binary. A lower estimate of 10%–50% and 20%–55% for the fraction of (nearly) equal-sized contact binaries is calculated in the 5:3 and 7:4 resonances, respectively. Surface colors of 2004 SC$_{60}$, 2013 BN$_{82}$, 2014 OL$_{394}$, and 2015 FP$_{345}$ have been obtained. Including these colors with ones from the literature reveals that elongated objects and contact binaries share the same ultrared surface color, except Manwë–Thorondor and 2004 SC$_{60}$. Not only are the colors of the 7:4 and 5:3 TNOs similar to the cold classicals, but we demonstrate that the rotational properties of the 5:3 and 7:4 resonants are similar to those of the cold classicals, inferring a clear link between these subpopulations.

Unified Astronomy Thesaurus concepts: Trans-Neptunian objects (1705); Resonant Kuiper belt objects (1396); Light curves (918)

Supporting material: machine-readable table

1. Introduction

Our solar system's outer regions are home to the trans-Neptunian objects (TNOs), which are small icy leftovers from the era of planet formation. Some of these planetesimals got caught in resonances with Neptune as this planet migrated through the solar system (Malhotra 1995; Levison et al. 2008; Gladman et al. 2012; Lawler et al. 2019; Volk & Malhotra 2019; Nesvorný 2021; Pirani et al. 2021; Nesvorný et al. 2022). A small body is in Neptune's resonance if its orbital period is in a specific ratio to Neptune's orbital period. As an example, a TNO in the 5:3 resonance will orbit three times around the Sun while Neptune will make five revolutions around the Sun in the same amount of time.

Several resonances are located within the classical trans-Neptunian belt, which is between ~40 and ~47 au. The main resonances in the classical population are the 5:3 and 7:4 (the main focus of this work), but there are also several higher-order resonances, the 8:5, 9:5, 17:9, and 15:8, among others (Gladman et al. 2008; Bannister et al. 2018). The Deep Ecliptic Survey (DES[3]) lists 59 and 76 TNOs in the 5:3 and 7:4 resonances, respectively, whereas higher-order resonances have a handful of detected objects so far (Figure 1). During Neptune's migration, objects formed at different heliocentric distances got pushed to the solar system's outer edge, and some of them ended up stuck into resonances, but it is also important to point out that due to the 5:3 and 7:4 locations, the classical belt plays a significant role by supplying objects into these resonances.

Murray-Clay & Schlichting (2011) proposed the migration-induced capture scenario in which TNOs can be captured into resonances. This scenario suggested that the 2:1 resonant TNOs at low inclinations should have a higher fraction of binaries compared to the 2:1 resonant TNOs at high inclinations, whereas the TNOs at low inclination in the 3:2 resonance should have a low fraction of binaries, as this resonance did not pass over the cold classical population. Both predictions were confirmed observationally and are discussed in the review paper by Noll et al. (2020). Murray-Clay & Schlichting (2011) also predicted that the 3:2 and 2:1 resonances should have a low-inclination cold classical component. Sheppard (2012) demonstrated that up to an inclination (i) of 10°, resonant TNOs are mainly from the dynamically cold classical population, whereas at $i > 10°$, the objects' main source is the dynamically hot classical population. However, Sheppard's (2012) conclusions are based only on color differences between the high-/low-inclination resonant TNOs and color alikeness with the cold classicals. One may wonder if the differences/similarities between the resonant and cold classical TNOs extend to other physical and rotational properties.

To complement our global picture of the resonant TNOs within the classical belt, we conduct a photometric survey to

---

[3] https://www.boulder.swri.edu/buie/kbo/desclass.html

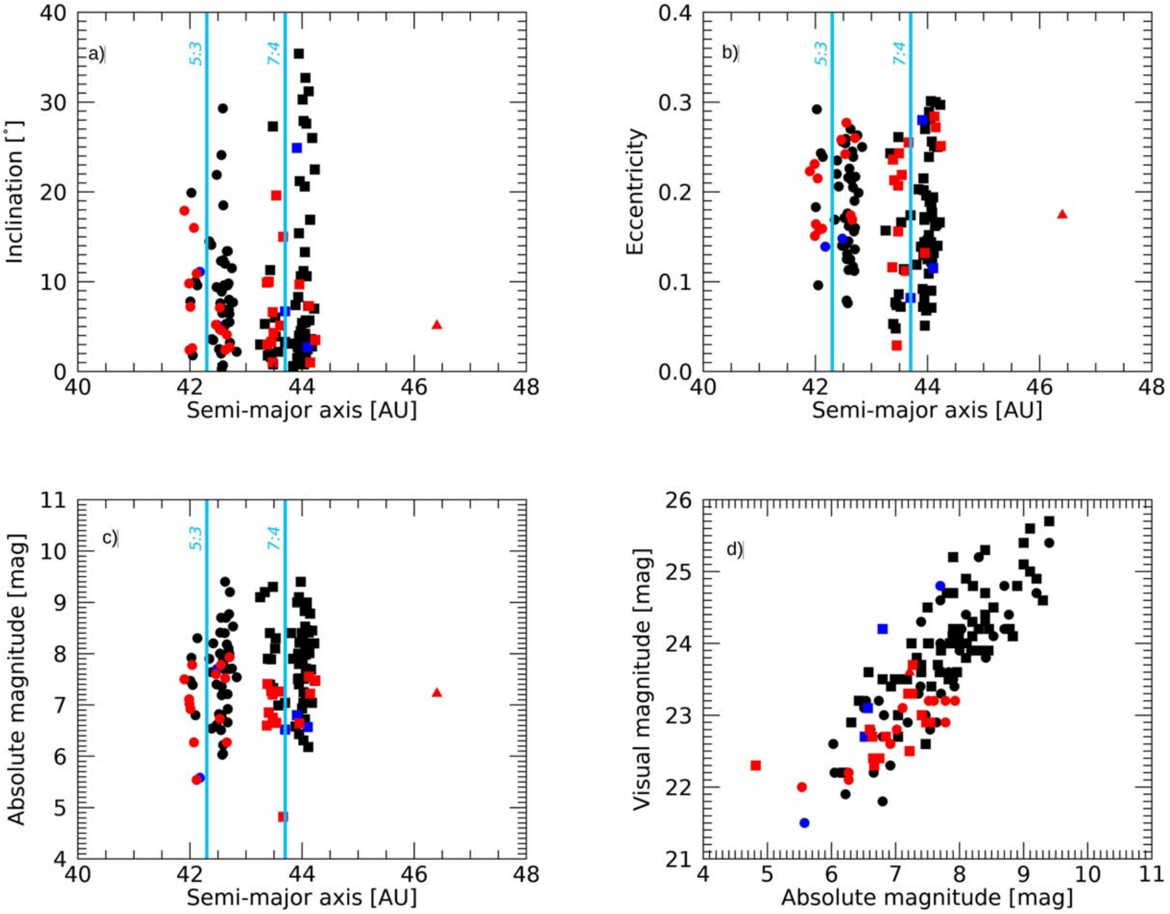

Figure 1. TNOs trapped in the 5:3 (circles) and 7:4 (squares) resonances with Neptune based on the DES classification are plotted with the following legend: black symbols for TNOs never observed for lightcurve studies, blue symbols for TNOs with some photometric information in the literature (Table 3), and red symbols for TNOs observed during our survey (Table 1). The red triangle corresponds to the object 2003 SP_{317}, whose dynamical classification is 17:9 resonant or classical TNO. Note that our survey targeted 2008 CS_{190} and 2001 XP_{254} (plotted with red symbols), which have been studied as well by Kecskeméthy et al. (2023).

obtain lightcurves, contact binary fractions, and amplitude and period distributions of the 5:3 and 7:4 resonances to infer the differences and similarities of these resonances with the dynamically cold classical population.

2. Our Survey: Telescopes, Instruments, and Strategy

We report a photometric study carried out from 2016 September to 2023 June with the 6.5 m Magellan-Baade telescope at the Las Campanas Observatory, Chile, and the 4.3 m Lowell Discovery Telescope (LDT) next to Happy Jack in Arizona, USA. This combination of medium-to-large facilities allows us to observe objects in the Southern and Northern Hemispheres down to a visual magnitude of about 23–24 mag. At both sites, we use their imager instruments: the wide-field imager called Inamori-Magellan Areal Camera and Spectrograph with a $27'.4$ diameter field for a $0''.20$ pixel^{-1} scale at the Magellan-Baade Telescope and the Large Monolithic Imager with a $12'.5 \times 12'.5$ field of view for a $0''.12$ pixel^{-1} scale at the LDT. For lightcurve observations, we select broadband filters (the *VR* filter at LDT and the WB4800–7800 filter at Magellan-Baade) aiming to increase the small body's signal-to-noise ratio. For surface color studies, we choose the *g'r'i'* Sloan filters. Exposure times are adapted to the facility, filter, weather/seeing conditions, and target brightness.

We select 5:3 and 7:4 resonant TNOs with a visual magnitude $V \lesssim 23$–23.5 mag encompassing a variety of inclinations, eccentricities, and absolute magnitudes (i.e., sizes). All objects targeted by our survey,[4] 13 in the 5:3 and 14 in the 7:4, are highlighted in Figure 1 and summarized in Table 1. The TNO (385458) 2003 SP_{317} is also in our target list, but its dynamical classification is questionable. With a semimajor axis of 46.405 au, an inclination of $5^{\circ}.1$, and an eccentricity of 0.174, it is a classical TNO for the DES,[5] but Alexandersen et al. (2019) classify it as a 17:9 resonant. Because of this classification issue, we do not plot the other classical or the other 17:9 TNOs in Figure 1, and 2003 SP_{317} will remain as an isolated object for this work.

During each observing night, we obtain dome flats and/or sky flats and biases to calibrate our science images. To optimize our observing time, we observe three to five objects alternatively on the same night to obtain their sparse lightcurves. With one image per object every 40–45 minutes or so for several hours, there is a good enough sampling to evaluate the lower limits of the object's period and variability. Ideally

---

[4] For this work, all orbital elements and visual and absolute magnitudes were extracted in 2023 February from the Minor Planet Center webpages: https://minorplanetcenter.net/iau/lists/t_tnos.html and https://minorplanetcenter.net/iau/lists/t_centaurs.html.

[5] https://www.boulder.swri.edu/buie/kbo/astrom/385458.html. For more details about the DES, see Elliot et al. (2005).

Table 1

Circumstances of Observing Runs as well as Rotational Period and Lightcurve Amplitude Estimates

Object	Date (UT)	r_h (au)	Δ (au)	α (deg)	Filter	Telescope	$P_{\rm rot}$ (hr)	Δm (mag)	$H_{\rm MPC}$ (mag)	a (au)	e	i (deg)	Wide Binary?[b]
						Mean-motion Resonance: 5:3							
(612086) 1999 CX$_{131}$	02/13/2021	37.138	38.086	0.4	VR	LDT	⋯	~0.1	7.11	41.986	0.231	9.8	No
(503883) 2001 QF$_{331}$	09/25/2016	32.338	31.376	0.5	VR	LDT	8.63 ± 0.04	0.45 ± 0.03	7.93	42.707	0.260	2.7	?
	09/25/2022	30.939	31.806	0.9	VR	LDT	⋯	⋯	⋯	⋯	⋯	⋯	⋯
	09/26/2022	30.930	31.805	0.9	VR	LDT	⋯	⋯	⋯	⋯	⋯	⋯	⋯
	09/30/2022	30.899	31.805	0.8	VR	LDT	⋯	⋯	⋯	⋯	⋯	⋯	⋯
(469420) 2001 XP$_{254}$	01/18/2021	32.251	33.171	0.6	VR	LDT	>6	>0.12	7.78	42.040	0.215	2.6	Yes
(149349) 2002 VA$_{131}$	02/08/2021	35.697	35.814	1.6	VR	LDT	>6	>0.05	6.73	42.533	0.242	7.1	No
	01/27/2022	35.262	35.615	1.5	VR	LDT	⋯	⋯	⋯	⋯	⋯	⋯	⋯
2002 VV$_{130}$	02/08/2021	35.398	35.444	1.6	VR	LDT	>3	>0.14	7.52	42.629	0.174	2.4	No
	11/27/2021	34.438	35.407	0.3	VR	LDT	>8	>0.14	⋯	⋯	⋯	⋯	⋯
	12/19/2022	34.521	35.363	0.8	VR	LDT	>3.5	>0.12	⋯	⋯	⋯	⋯	⋯
(469584) 2003 YW$_{179}$	01/18/2021	35.311	36.205	0.7	VR	LDT	15.41 ± 0.03	0.58 ± 0.02	7.02	41.992	0.151	2.4	No
	01/27/2022	35.337	36.276	0.5	VR	LDT	⋯	⋯	⋯	⋯	⋯	...	⋯
	03/10/2022	35.385	36.283	0.7	VR	LDT	⋯	⋯	⋯	⋯	⋯	...	⋯
	03/26/2022	35.536	36.286	1.0	VR	LDT	⋯	⋯	⋯	⋯	⋯	...	⋯
	04/03/2022	35.635	36.288	1.2	VR	LDT	⋯	⋯	⋯	⋯	⋯	...	⋯
	02/12/2023	35.368	36.353	0.1	VR	LDT	⋯	⋯	⋯	⋯	⋯	...	⋯
2004 VE$_{131}$	01/18/2021	34.901	35.512	1.3	VR	LDT	>5.5	>0.17	7.6	42.463	0.258	5.2	No
	02/08/2021	35.209	35.499	1.5	VR	LDT	>3.5	>0.28	⋯	⋯	⋯	⋯	⋯
	11/27/2021	34.333	35.317	0.1	VR	LDT	>7	>0.34	⋯	⋯	⋯	⋯	⋯
	12/03/2021	34.329	35.313	0.1	VR	LDT	>8	>0.40	⋯	⋯	⋯	⋯	⋯
	12/05/2021	34.331	35.312	0.1	VR	LDT	>7	>0.40	⋯	⋯	⋯	⋯	⋯
(434709) 2006 CJ$_{69}$	02/08/2021	32.263	33.152	0.7	VR	LDT	23.39 ± 0.07	0.35 ± 0.04	7.50	41.901	0.223	17.9	?
	02/13/2021	32.229	33.151	0.6	VR	LDT	⋯	⋯	⋯	⋯	⋯	⋯	⋯
	04/13/2021	32.386	33.135	1.2	VR	LDT	⋯	⋯	⋯	⋯	⋯	⋯	⋯
	01/27/2022	32.299	33.060	1.1	VR	LDT	⋯	⋯	⋯	⋯	⋯	⋯	⋯
	04/01/2022	32.165	33.044	0.8	VR	LDT	⋯	⋯	⋯	⋯	⋯	⋯	⋯
	04/03/2022	32.179	33.044	0.9	VR	LDT	⋯	⋯	⋯	⋯	⋯	⋯	⋯
(470523) 2008 CS$_{190}$	02/28/2019	36.252	37.233	0.2	WB	Magellan	⋯	~0.1	6.27	42.071	0.158	16.0	No
	03/01/2019	36.250	37.234	0.2	WB	Magellan	⋯	⋯	⋯	⋯	⋯	⋯	⋯
	03/02/2019	36.249	37.234	0.2	WB	Magellan	⋯	⋯	⋯	⋯	⋯	⋯	⋯
2012 BY$_{154}$	02/28/2019	34.684	35.655	0.3	WB	Magellan	⋯	~0.1	6.92	42.008	0.164	7.2	?
	03/02/2019	34.677	35.655	0.3	WB	Magellan	⋯	⋯	⋯	⋯	⋯	⋯	⋯
(523688) 2014 DK$_{143}$	05/14/2021	42.730	43.714	0.3	VR	LDT	8.99 ± 0.03	0.21 ± 0.03	5.54	42.120	0.159	10.9	?
	04/21/2023	43.161	43.990	0.7	VR	LDT	⋯	⋯	⋯	⋯	⋯	⋯	⋯
	04/22/2023	43.152	43.990	0.7	VR	LDT	⋯	⋯	⋯	⋯	⋯	⋯	⋯
	04/25/2023	43.127	43.992	0.7	VR	LDT	⋯	⋯	⋯	⋯	⋯	⋯	⋯
	04/27/2023	43.112	43.992	0.6	VR	LDT	⋯	⋯	⋯	⋯	⋯	⋯	⋯
	06/18/2023	43.097	44.012	0.6	$g'r'i'$	LDT	⋯	⋯	⋯	⋯	⋯	⋯	⋯
(523731) 2014 OK$_{394}$	02/12/2023	36.846	37.007	1.5	VR	LDT	>4	>0.05	6.27	42.587	0.169	4.1	?
(543734) 2014 OL$_{394}$	09/25/2016	30.775	29.825	0.6	VR	LDT	>4	>0.28	7.78	42.554	0.277	4.6	?
	10/28/2017	30.785	29.811	0.4	VR	LDT	>4	>0.41	⋯	⋯	⋯	⋯	⋯
	10/16/2023	30.120	31.081	0.5	$g'r'i'$	LDT	⋯	⋯	⋯	⋯	⋯	⋯	⋯

Table 1
(Continued)

Object	Date (UT)	r_h (au)	Δ (au)	α (deg)	Filter	Telescope	$P_{\rm rot}$ (hr)	Δm (mag)	$H_{\rm MPC}$ (mag)	a (au)	e	i (deg)	Wide Binary?[b]
Mean-motion Resonance: 7:4													
1999 HG$_{12}$	04/22/2023	38.727	39.631	0.6	WB	Magellan	>5	>0.18	7.2	43.968	0.160	1.0	No
(129772) 1999 HR$_{11}$	05/16/2018	42.177	41.224	0.5	WB	Magellan	>7	>0.17	7.27	43.450	0.029	3.3	?
	05/17/2018	42.177	41.229	0.5	WB	Magellan	⋯	⋯	⋯	⋯	⋯	⋯	⋯
(118378) 1999 HT$_{11}$	04/25/2023	38.664	39.566	0.7	VR	LDT	>3	>0.52	7.26	43.773	0.115	5.1	No
	04/27/2023	38.649	39.566	0.6	VR	LDT	>3.5	>0.44	⋯	⋯	⋯	⋯	⋯
(60620) 2000 FD$_8$[a]	04/04/2021	35.308	36.214	0.7	VR	LDT	>2	>0.09	6.65	43.690	0.222	19.5	No
	05/14/2021	35.245	36.196	0.5	VR	LDT	>2	>0.03	⋯	⋯	⋯	⋯	
(385527) 2004 OK$_{14}$	07/03/2017	34.304	33.540	1.1	VR	LDT	⋯	∼0.1	7.48	44.236	0.251	3.5	No
2004 OQ$_{15}$[a]	07/02/2017	38.379	39.278	0.7	VR	LDT	>2	>0.28	6.64	43.952	0.132	9.7	?
2004 SC$_{60}$	10/03/2019	31.702	32.669	0.5	VR	LDT	58.09 ± 0.08	0.44 ± 0.04	7.22	44.145	0.272	1.0	?
	10/06/2019	31.690	32.669	0.4	VR	LDT	⋯	⋯	⋯	⋯	⋯	...	⋯
	12/01/2019	31.949	32.653	1.2	WB	Magellan	⋯	⋯	⋯	⋯	⋯	...	⋯
	12/02/2019	31.961	32.653	1.2	WB	Magellan	⋯	⋯	⋯	⋯	⋯	...	⋯
	09/24/2020	31.669	32.576	0.8	VR	LDT	⋯	⋯	⋯	⋯	⋯	...	⋯
	09/13/2021	31.704	32.492	1.1	VR	LDT	⋯	⋯	⋯	⋯	⋯	...	⋯
	09/30/2022	31.497	32.411	0.7	VR	LDT	⋯	⋯	⋯	⋯	⋯	⋯	⋯
	10/16/2023	31.359	32.339	0.3	$g'r'i'$	LDT	⋯	⋯	⋯	⋯	⋯	⋯	⋯
(531917) 2013 BN$_{82}$	02/08/2021	34.114	35.095	0.2	VR	LDT	18.22 ± 0.04	0.40 ± 0.04	6.73	43.478	0.207	6.6	?
	02/13/2021	34.122	35.097	0.3	VR	LDT	⋯	⋯	⋯	⋯	⋯	⋯	⋯
	03/08/2021	34.251	35.102	0.8	VR	LDT	⋯	⋯	⋯	⋯	⋯	⋯	⋯
	03/10/2022	34.341	35.194	0.8	VR	LDT	⋯	⋯	⋯	⋯	⋯	⋯	⋯
	03/26/2022	34.512	35.198	1.2	VR	LDT	⋯	⋯	⋯	⋯	⋯	⋯	⋯
	03/27/2023	34.596	35.297	1.2	$g'r'i'$	LDT	⋯	⋯	⋯	⋯	⋯	⋯	⋯
(532039) 2013 FR$_{28}$	03/01/2019	33.588	34.252	1.2	WB	Magellan	13.97 ± 0.04	0.94 ± 0.02	7.41	43.384	0.236	3.0	?
	03/02/2019	33.575	34.253	1.2	WB	Magellan	⋯	⋯	⋯	⋯	⋯	⋯	⋯
	05/04/2019	33.304	34.275	0.5	VR	LDT	⋯	⋯	⋯	⋯	⋯	⋯	⋯
	05/19/2020	33.535	34.412	0.9	VR	LDT	⋯	⋯	⋯	⋯	⋯	⋯	⋯
	05/20/2020	33.544	34.413	0.9	VR	LDT	⋯	⋯	⋯	⋯	⋯	⋯	⋯
2013 SJ$_{102}$	09/24/2020	31.579	32.526	0.6	VR	LDT	⋯	∼0.1	7.55	44.124	0.284	7.3	?
(533028) 2014 AL$_{55}$	03/18/2017	35.432	34.781	1.2	VR	LDT	>3	>0.11	6.67	43.492	0.243	4.3	?
	02/08/2021	33.752	34.736	0.1	VR	LDT	⋯	⋯	⋯	⋯	⋯	⋯	⋯
(523742) 2014 TZ$_{85}$	02/12/2023	53.419	54.308	0.5	VR	LDT	>4	>0.08	4.82	43.662	0.255	15.0	?
(559179) 2015 BR$_{518}$	03/02/2020	39.440	40.364	0.5	VR	LDT	>3.5	>0.06	6.60	43.379	0.114	9.9	?
	02/13/2021	39.683	40.452	0.9	VR	LDT	>5	>0.14	⋯	⋯	⋯	⋯	⋯
(536922) 2015 FP$_{345}$	05/04/2019	35.228	36.196	0.5	VR	LDT	8.47 ± 0.02	0.52 ± 0.04	6.85	43.407	0.213	10.0	?
	03/02/2020	35.702	36.323	1.2	VR	LDT	⋯	⋯	⋯	⋯	⋯	⋯	⋯
	05/19/2020	35.464	36.356	0.8	VR	LDT	⋯	⋯	⋯	⋯	⋯	⋯	⋯
	05/20/2020	35.472	36.356	0.8	VR	LDT	⋯	⋯	⋯	⋯	⋯	⋯	⋯
	03/17/2021	35.711	36.486	1.0	VR	LDT	⋯	⋯	⋯	⋯	⋯	⋯	⋯
	03/18/2021	35.700	36.486	1.0	WB	Magellan	⋯	⋯	⋯	⋯	⋯	⋯	⋯
	03/21/2021	35.671	36.487	0.9	WB	Magellan	⋯	⋯	⋯	⋯	⋯	⋯	⋯
	05/25/2022	35.799	36.677	0.8	$g'r'i'$	LDT	⋯	⋯	⋯	⋯	⋯	⋯	⋯

Table 1
(Continued)

Object	Date (UT)	r_h (au)	Δ (au)	α (deg)	Filter	Telescope	$P_{\rm rot}$ (hr)	Δm (mag)	$H_{\rm MPC}$ (mag)	a (au)	e	i (deg)	Wide Binary?[b]
Mean-motion Resonance: 17:9 (or Classical TNO)													
(385458) 2003 SP_{317}	10/17/2020	41.260	42.239	0.3	VR	LDT	12.39 ± 0.03	0.85 ± 0.03	7.22	46.405	0.174	5.1	No
	09/25/2022	40.983	41.953	0.4	VR	LDT	…	…	…	…	…	…	…
	09/26/2022	40.978	41.953	0.3	VR	LDT	…	…	…	…	…	…	…
	09/30/2022	40.964	41.951	0.2	VR	LDT	…	…	…	…	…	…	…

Notes.

[a] Both objects are probably 7:4 resonants, but other dynamical classifications are possible: https://www.boulder.swri.edu/~buie/kbo/astrom/04OQ15.html and https://www.boulder.swri.edu/~buie/kbo/astrom/60620.html.

[b] Objects were imaged by HST programs 9060, 10514, 10800, 11113, and 12468 (K. S. Noll et al.), 11644 (M. E. Brown et al.), and 13664 (S. D. Benecchi et al.).

(weather- and observing-schedule-dependent), we reschedule the objects on at least one different night to confirm the first sparse lightcurve results. If an object displays a moderate/large variability ($\Delta m \gtrsim 0.3$ mag), it will be reobserved over several nights to derive its full lightcurve. All our science images are reduced and analyzed with the standard steps described in Thirouin et al. (2010, 2014). Basically, we obtain the aperture photometry of our targets followed by a periodicity search such as the Lomb periodogram (Lomb 1976). The Lomb periodogram's highest peak gives the strongest periodicity detected in the data set, but the proper rotational period can be a multiple of the detected period. Assuming a single-peaked lightcurve, the true period of the object will be the one favored by the Lomb periodogram, but if the lightcurve is double-peaked, then the true rotational period is twice the one favored by the periodogram. Thirouin et al. (2014) showed that a spheroidal object has a low-amplitude single-peaked lightcurve, whereas an elongated object as well as contact binaries have moderate-to-high-amplitude double-peaked lightcurves (more details in the next section).

3. Lightcurve Interpretations

Based on Leone et al. (1984), Sheppard & Jewitt (2004) proposed a "lightcurve classification" using rotational period (P) and lightcurve amplitude (Δm) to infer if a lightcurve is due to albedo difference(s) on the body's surface, and/or due to a nonspherical object, and/or if the object is, in fact, a binary system. Three regions were identified (see Figure 5 in Sheppard & Jewitt 2004): in region A, a small lightcurve amplitude ($\Delta m < 0.25$ mag) could be caused by an elongated object, albedo, or binarity; in region B, a moderate-to-large lightcurve amplitude ($\Delta m > 0.25$ mag) with a fast rotation is most likely due to a rotational elongated object; and in region C, a moderate-to-large lightcurve amplitude with an average or slow rotation is most likely due to a nearly equal-sized binary. Sheppard & Jewitt (2004) adopted a cutoff at $\Delta m = 0.25$ mag, but this limit was revaluated at about 0.15 mag by Thirouin et al. (2010). Below, we will use a threshold of 0.20 mag, which is in between both estimates.

Additional criteria like the morphology of the lightcurve can be used to complement the Sheppard & Jewitt (2004) classification. Lacerda & Jewitt (2007) and Lacerda et al. (2008) showed that an elongated triaxial (Jacobi ellipsoid) object has a sinusoidal[6] lightcurve with a moderate variability (typically between 0.2 and 0.4 mag), but a spherical object (McLaurin spheroid) with/without albedo disparity on its surface has a low/flat amplitude (typically lower than 0.2 mag), whereas a nearly equal-sized contact binary lightcurve has a large amplitude with an inverted U shape at the maximum of brightness and a V shape at the minimum of brightness (i.e., nonsinusoidal lightcurve) from shadowing effects between the components. However, the U/V shapes can be less obvious if the contact binary is not observed equator-on. The modeling of the contact binary 2001 QG$_{298}$ by Lacerda (2011) illustrates how the system's geometry affects the morphology and amplitude of a contact binary's lightcurve.

According to Jeans (1919), Weidenschilling (1980), Leone et al. (1984), and Chandrasekhar (1987), a triaxial object[7] with an axis ratio $a/b = 2.3$ is unstable due to rotational fission, meaning that this object is so "stretched" that as it rotates it will break into two components, creating a close/contact binary system. Considering an equatorial view ($\xi = 90°$), the lightcurve amplitude and axis ratio are related,

$$\Delta m = 2.5 \log\left(\frac{a}{b}\right), \tag{2}$$

and so an axis ratio of 2.3 corresponds to an amplitude of 0.9 mag. Therefore, we consider objects whose lightcurves have $\Delta m \geqslant 0.9$ mag as the *most likely* contact binaries. However, if the viewing geometry is not equatorial ($\xi \neq 90°$),

$$\Delta m = 2.5 \log\left(\frac{a}{b}\right) - 1.25 \log\left(\frac{a^2 \cos^2 \xi + c^2 \sin^2 \xi}{b^2 \cos^2 \xi + c^2 \sin^2 \xi}\right), \tag{3}$$

then an object with $a/b = 2.3$ will have an amplitude smaller than 0.9 mag. Therefore, a lightcurve with an indication of a V/U shape (nonsinusoidal lightcurve) and a large amplitude can also be caused by a contact binary, even if the threshold at 0.9 mag is not reached. An object with a nonsinusoidal large-amplitude lightcurve and a Fourier series chi-square (χ^2) value above 1 is a *likely* contact binary when the 0.9 mag limit is not met. In the case of a likely contact binary, only a lightcurve at a significantly different epoch of at least four or more years (depending on the obliquity of the system) and system modeling will confirm the system's characteristics (Lacerda 2011; Lacerda et al. 2014b).

In some instances, only a partial lightcurve with lower limits for the periodicity and object's variability can be available, and thus the presence of a V/U shape can be difficult/impossible to identify. If the object displays a large variability, it is a *potential* contact binary, and additional observations are required to confirm this conclusion.

In this paper, we consider that a close/contact binary can be a small body with a bilobed shape or two objects touching at one point, as well as two objects with a small separation of less than a few hundred kilometers. Following Nesvorný & Vokrouhlický's (2019) definition, a contact binary/close binary has $a_B/R_B < 10$, where a_B is the binary semimajor axis and $R_B^3 = R_{\text{primary}}^3 + R_{\text{secondary}}^3$, with R_{primary} and $R_{\text{secondary}}$ being the radii of the system's components.

In the following, we will interpret all sinusoidal lightcurves as being caused by elongated small bodies. But we point out that for these bodies, a lightcurve at a different epoch is warranted to discard a future contact-binary-shaped lightcurve. A nearly equal-sized contact binary not imaged nearly edge-on may not display signs of U/V shapes, and so only a new lightcurve at a different epoch can determine the object's shape.

4. Lightcurve Results

Below, the rotational and physical properties of the 28 TNOs observed during our survey will be discussed (Tables 1 and 2). The entire photometry and partial/flat lightcurves are in Appendicies A and B (see Table 7 in Appendix B). For each complete lightcurve study, we report the Lomb periodogram (plot (a) on the upcoming figures) described in Section 2 and

---

[6] A second-order Fourier series can fit a sinusoidal lightcurve, but it will not fit a contact binary lightcurve. The formula for a second-order Fourier series fit is

$$\text{Fit}_{\text{Fourier}} = a + b\cos(2\pi\phi) + c\sin(2\pi\phi) + d\cos(4\pi\phi) + e\sin(4\pi\phi), \tag{1}$$

with ϕ as the rotational phase and a, b, c, d, and e as constants.

[7] Triaxial object with axes $a > b > c$, rotating along the c-axis.

Table 2
Properties Derived from the Lightcurve of the Contact Binaries and Elongated Objects (Only Objects with a Full Lightcurve)

Object	q	ρ (g cm^{-3})	$\frac{b}{a}$	$\frac{c}{a}$	$\frac{b'}{a'}$	$\frac{c'}{a'}$	D	Alb.	∅ (km)	a (km)	b (km)	c (km)	a' (km)	b' (km)	c' (km)	d (km)
Most Likely and Likely Contact Binaries																
2003 SP$_{317}$	0.75	1	0.85	0.78	0.79	0.73	0.77	0.04	239	74	63	57	70	56	51	187
	⋯	⋯	⋯	⋯	⋯	⋯	⋯	0.20	107	33	28	26	32	25	23	84
	1	1.25	0.86	0.81	0.79	0.75	0.69	0.04	239	69	59	56	73	58	55	205
	⋯	⋯	⋯	⋯	⋯	⋯	⋯	0.20	107	31	27	25	33	26	24	92
2004 SC$_{60}$	0.4	1	1	1	1	1	0.25	0.04	239	67	67	67	53	53	53	478
	⋯	⋯	⋯	⋯	⋯	⋯	⋯	0.20	107	30	30	30	24	24	24	214
2006 CJ$_{69}$	0.2	1	0.99	0.96	0.84	0.83	0.50	0.04	210	68	67	65	44	37	37	224
	⋯	⋯	⋯	⋯	⋯	⋯	⋯	0.20	94	30	30	29	20	17	16	100
2013 BN$_{82}$	0.3	1	0.97	0.93	0.90	0.86	0.51	0.04	300	94	91	87	67	60	57	315
	⋯	⋯	⋯	⋯	⋯	⋯	⋯	0.20	134	42	41	39	30	27	26	141
2013 FR$_{28}$	1	1	0.87	0.81	0.80	0.75	0.68	0.04	219	63	54	51	67	53	50	190
	⋯	⋯	⋯	⋯	⋯	⋯	⋯	0.20	98	28	24	23	30	24	22	85
Elongated Objects, $\xi = 90°$																
2001 QF$_{331}$	⋯	>0.56	0.66	0.46	⋯	⋯	⋯	0.04	172	139	92	42	⋯	⋯	⋯	⋯
	⋯	⋯	⋯	⋯	⋯	⋯	⋯	0.20	77	62	41	19	⋯	⋯	⋯	⋯
2003 YW$_{179}$	⋯	>0.18	0.59	0.43	⋯	⋯	⋯	0.04	262	224	132	57	⋯	⋯	⋯	⋯
	⋯	⋯	⋯	⋯	⋯	⋯	⋯	0.20	117	100	59	25	⋯	⋯	⋯	⋯
2014 DK$_{143}$	⋯	>0.49	0.82	0.53	⋯	⋯	⋯	0.04	518	373	306	162	⋯	⋯	⋯	⋯
	⋯	⋯	⋯	⋯	⋯	⋯	⋯	0.20	232	167	137	73	⋯	⋯	⋯	⋯
2015 FP$_{345}$	⋯	>0.59	0.62	0.44	⋯	⋯	⋯	0.04	283	237	147	65	⋯	⋯	⋯	⋯
	⋯	⋯	⋯	⋯	⋯	⋯	⋯	0.20	127	106	66	29	⋯	⋯	⋯	⋯
Elongated Objects, $\xi = 60°$																
2001 QF$_{331}$	⋯	>0.58	0.59	0.43	⋯	⋯	⋯	0.04	172	147	87	37	⋯	⋯	⋯	⋯
	⋯	⋯	⋯	⋯	⋯	⋯	⋯	0.20	77	66	39	17	⋯	⋯	⋯	⋯
2003 YW$_{179}$	⋯	>0.19	0.52	0.40	⋯	⋯	⋯	0.04	262	238	124	49	⋯	⋯	⋯	⋯
	⋯	⋯	⋯	⋯	⋯	⋯	⋯	0.20	117	106	55	22	⋯	⋯	⋯	⋯
2014 DK$_{143}$	⋯	>0.50	0.74	0.49	⋯	⋯	⋯	0.04	518	397	294	144	⋯	⋯	⋯	⋯
	⋯	⋯	⋯	⋯	⋯	⋯	⋯	0.20	232	178	131	64	⋯	⋯	⋯	⋯
2015 FP$_{345}$	⋯	>0.62	0.55	0.41	⋯	⋯	⋯	0.04	283	251	138	57	⋯	⋯	⋯	⋯
	⋯	⋯	⋯	⋯	⋯	⋯	⋯	0.20	127	113	62	25	⋯	⋯	⋯	⋯

Note. For the contact binaries: mass ratio (q); density (ρ); axis ratios of the primary and secondary (abc and $a'b'c'$, respectively); $D = (a + a')/d$, where d is the orbital separation as defined by Leone et al. (1984) with $D = 1$ if the two objects are in contact; albedo (Alb.); and diameter (∅). For the elongated objects: lower limit to the density and axis ratios derived with two different viewing angles (ξ). The objects' albedos are unknown; thus, we use two default values of 0.04 and 0.20 (Lacerda et al. 2014a).

the lightcurve with a rotational phase between 0 and 1.2 on plot (b).

4.1. Objects with Δm $\geqslant$ 0.9 mag

(532039) 2013 FR$_{28}$—With the Magellan-Baade telescope and the LDT, we observed this TNO in 2019 and 2020. The periodogram prefers a frequency of $f = 3.44$ cycles day^{-1} equivalent to a period of $P = 6.99$ hr. Due to the lightcurve morphology, the object's rotation is double, so $P_{\text{rotational}}^{\text{double}} = 13.97 \pm 0.04$ hr. Our study concludes that 2013 FR$_{28}$ has a nonsinusoidal lightcurve with $\Delta m = 0.94 \pm 0.02$ mag (Figure 2). The Fourier series does not match our data because of the distinctive U and V shapes. Because of the morphology and amplitude above the 0.9 mag limit, 2013 FR$_{28}$ is a most likely contact binary.

Leone et al. (1984) studied the figures of equilibrium for binary systems that we can use for crude modeling to derive some basic information. Following their procedure, we derive that 2013 FR$_{28}$ has a mass ratio[8] $q \sim 1$ with $\rho \sim 1$ g cm^{-3}. The properties extracted from this modeling are available in Table 2. We can also infer based on this lightcurve that 2013 FR$_{28}$ is nearly equator-on (Lacerda 2011).

In the trans-Neptunian belt, such a well-sampled and extreme variability is only surpassed by the 3:2 resonant contact binary 2001 QG$_{298}$, whose variability was 1.14 ± 0.04 mag in 2002–2003 (Sheppard & Jewitt 2004). With the addition of 2013 FR$_{28}$, there are only two most likely trans-Neptunian contact binaries detected based on their peculiar lightcurve morphology and large amplitude over 0.9 mag. Further observations will allow its pole orientation and true maximum amplitude to be determined.

4.2. Objects with Δm between 0.5 and 0.9 mag

(385458) 2003 SP$_{317}$—We obtained images of 2003 SP$_{317}$ in 2020 and 2022 over four nights with the LDT. The periodogram's highest peak is at $f = 3.87$ cycles day^{-1} ($P = 6.20$ hr), but based on the lightcurve asymmetry and variability, a double-peaked period of 12.39 ± 0.03 hr is more appropriate (Figure 3). 2003 SP$_{317}$ has $\Delta m = 0.85 \pm 0.03$ mag.

Using the Hyper Suprime-Cam on the Subaru telescope, Alexandersen et al. (2019) observed 2003 SP$_{317}$ for short-term variability. They report an incomplete lightcurve with a periodicity of 12.45 hr, which is similar to the periodicity

---

[8] Because the error bars for the period and amplitude are not taken into account, we prefer to use approximate values for the density and mass ratio.

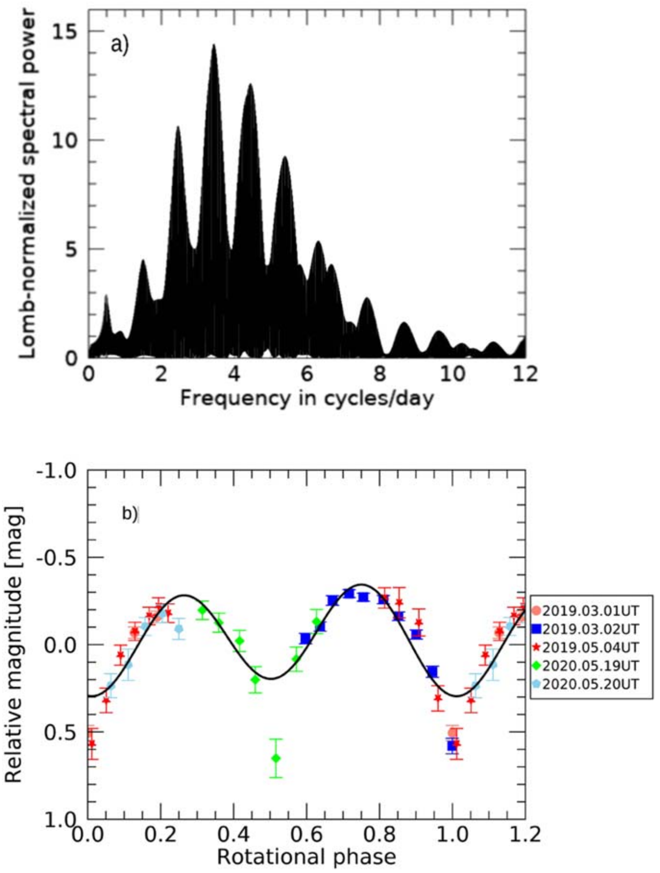

Figure 2. The main peak of the Lomb periodogram (plot (a)) is located at 3.44 cycles day^{-1}. The double-peaked lightcurve of 2013 FR_{28} with $P^{\mathrm{double}}_{\mathrm{rotational}} = 13.97 \pm 0.04$ hr has an amplitude larger than the cutoff at 0.9 mag and the V/U morphology of a most likely contact binary (plot (b)). The Fourier series fit (black solid line) cannot match the observations with $\chi^2 = 4.90$.

derived from our observations. They only sample the maximum of the curve over their two observing nights for an amplitude limit of 0.56 mag.

In Figure 3, we overplot a Fourier series fit to the lightcurve, but it is unable to reproduce the second minimum showing that the lightcurve of 2003 SP_{317} is not sinusoidal. The lightcurve presents the classical V shape of a contact binary but not the U shape. Because Δm is just below the 0.9 mag cutoff, we conclude that 2003 SP_{317} is a likely contact binary.

Following Leone et al. (1984), we estimate that 2003 SP_{317} has a mass ratio between $q_{\min} \sim 0.75$ with $\rho_{\min} \sim 1$ g cm^{-3} and $q_{\max} \sim 1$ with $\rho_{\max} \sim 1.25$ g cm^{-3} (Table 2).

4.2.1. (469584) 2003 YW_{179}

We observed this object in six instances from 2021 to 2023. The periodogram suggests a period of 3.12 cycles day^{-1}. As the symmetric lightcurve of 2003 YW_{179} has a large variability, the best rotational period is 15.41 ± 0.03 hr (Figure 4). We derive an amplitude of 0.58 ± 0.02 mag from the fit, which is in good agreement with the data. We conclude that 2003 YW_{179} is a highly elongated object with axis ratios such as $a/b = 1.71$ and $c/a = 0.43$ with a density $\rho > 0.18$ g cm^{-3} for a view of $\xi = 90°$ (Table 2). However, as for 2001 QF_{331}, additional lightcurves with amplitude changes are warranted to secure our interpretation.

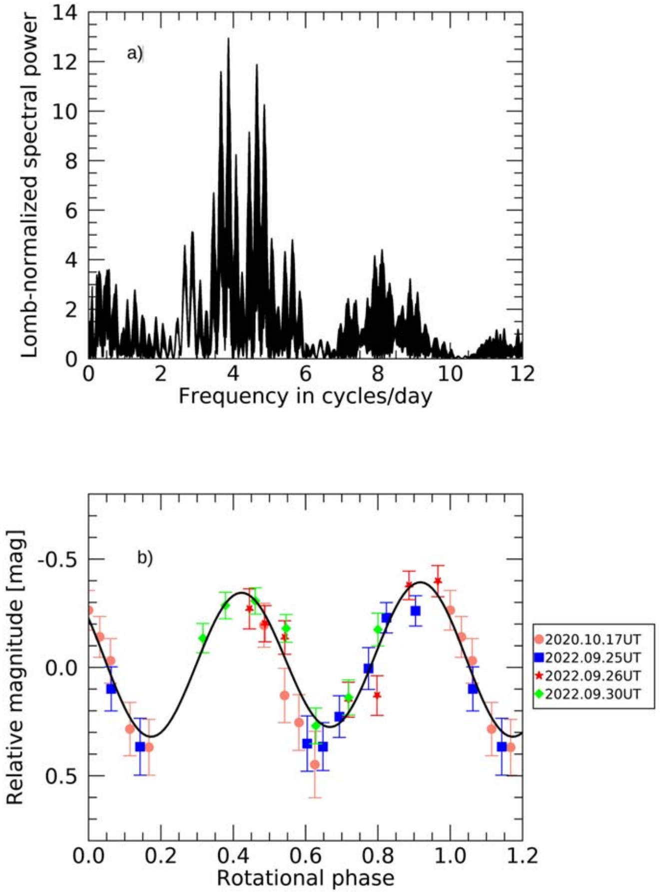

Figure 3. The lightcurve of 2003 SP_{317} is asymmetric and double-peaked with a period $P^{\mathrm{double}}_{\mathrm{rotational}} = 12.39 \pm 0.03$ hr and $\Delta m = 0.85 \pm 0.03$ mag. We classify this body as a likely contact binary due to its high variability and V shape at the minima and because the Fourier series fit is unable to reproduce the lightcurve ($\chi^2 = 1.02$).

4.2.2. (536922) 2015 FP_{345}

From 2019 to 2021, we imaged 2015 FP_{345} on eight occasions for short-term variability and once in 2022 for colors. In Figure 5, the period determination favors 5.66 cycles day^{-1}; as the lightcurve of 2015 FP_{345} is asymmetric, its true rotation is $P^{\mathrm{double}}_{\mathrm{rotational}} = 8.47 \pm 0.02$ hr. A second-order Fourier series nicely fits the lightcurve, and thus we conclude that 2015 FP_{345} is an elongated triaxial object with albedo variegation(s). An asymmetric lightcurve can be due to albedo marking(s) or an irregular shape. In the case of Haumea, Lacerda et al. (2008) demonstrated that a dark red spot is causing an asymmetric lightcurve. A topographic feature on 2003 AZ_{84} was discovered by Dias-Oliveira et al. (2017), but its lightcurve is symmetric. Therefore, we prefer the option of albedo spot(s) to explain an asymmetric lightcurve. Degewij et al. (1979), Jewitt & Sheppard (2002), Lacerda et al. (2008), and Thirouin et al. (2010) indicate that the asymmetry is due to albedo spot(s) that are typically between 4% and 10% on the TNO surfaces. The lightcurve amplitude is 0.52 ± 0.04 mag.

Considering an equatorial viewing geometry ($\xi = 90°$), the axis ratios of 2015 FP_{345} are $a/b = 1.61$ and $c/a = 0.44$ for a density $\rho > 0.59$ g cm^{-3} (Table 2).

In 2022 May, we imaged 2015 FP_{345} with three Sloan filters for surface colors that are $g' - i' = 1.34 \pm 0.07$ and $g' - r' = 0.88 \pm 0.07$ mag, making it an ultrared object (colors are discussed in Section 5.3).

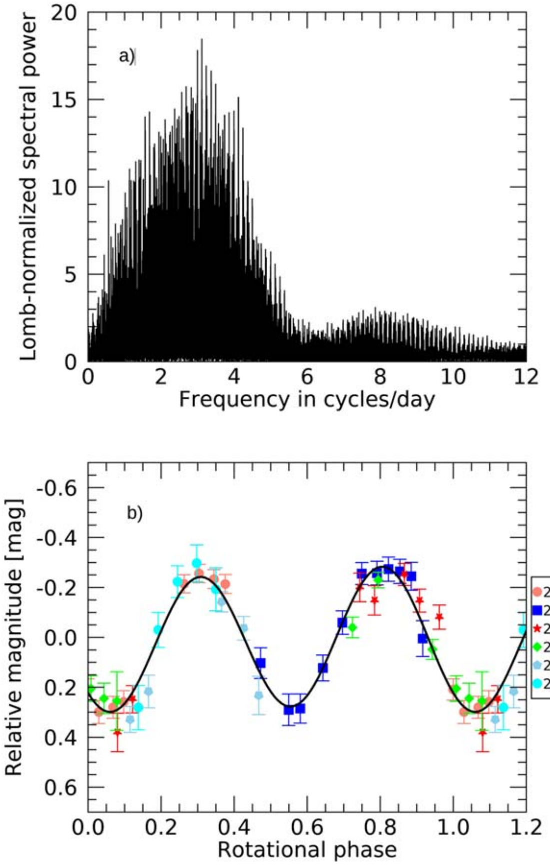

Figure 4. The periodogram's main peak is at 3.12 cycles day^{-1} (plot (a)). Because of the large photometric variability of 2003 YW$_{179}$, the double-peaked rotational period of 15.41 hr is best suited. A second-order Fourier fit (black curve) is a good match to our data sets inferring that this object is elongated (plot (b)).

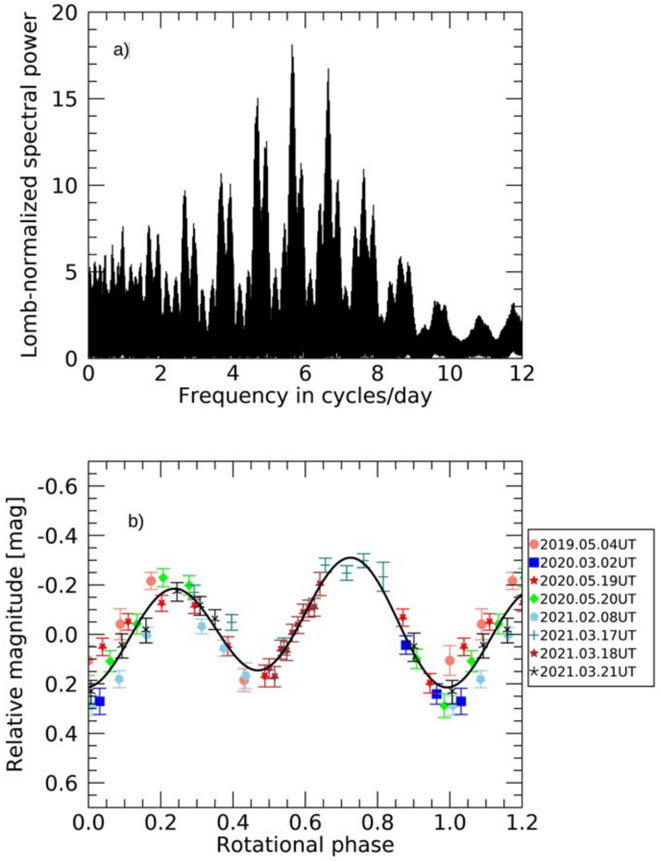

Figure 5. We infer that the lightcurve of 2015 FP$_{345}$ is double-peaked with $P^{\rm double}_{\rm rotational}$ = 8.47 ± 0.02 hr. This lightcurve is fitted by a Fourier series demonstrating that this object is elongated and likely has spot(s) on its surface.

4.2.3. (118378) 1999 HT$_{11}$

In 2023 April, we obtained two observing blocks of 3 and 3.5 hr for this object with the LDT. The photometry of 1999 HT$_{11}$ presents a higher uncertainty than the rest because it is one of the faintest targets in our sample and because of its high variability of 0.52 and 0.44 mag over the respective observing blocks. We do not have enough data to provide its complete lightcurve, but we consider 1999 HT$_{11}$ a potential contact binary due to its amplitude.

4.3. Objects with Δm between 0.3 and 0.5 mag

4.3.1. (503883) 2001 QF$_{331}$

We observed 2001 QF$_{331}$ over four nights with the LDT in 2016 and 2022. The periodicity search favors a frequency of 5.56 cycles day^{-1}. However, due to the object's large variability and also due to an asymmetric[9] lightcurve, the double-peaked solution is more appropriate for this object. We conclude that the period of 2001 QF$_{331}$ is 8.63 ± 0.04 hr (Figure 6). The Fourier series fits the lightcurve and infers that the amplitude from the tallest maximum to the deepest minimum is 0.45 ± 0.03 mag. The lightcurve interpretation suggests that 2001 QF$_{331}$ is not a nearly equal-sized contact binary imaged (nearly) edge-on but rather a single elongated object with some albedo variations on its surface. Only future observations to determine its pole orientation from amplitude changes can distinguish between an elongated object and a nearly equal-sized contact binary.

Assuming that small bodies have a fluidlike behavior and are in hydrostatic equilibrium, Chandrasekhar (1987) studied the figures of equilibrium for triaxial objects (among other object configurations), and, using his work, we can derive lower limits to the object's density and its axis ratios for a certain viewing angle (ξ): if $\xi = 90°$, $a/b = 1.51$, $c/a = 0.46$, and $\rho > 0.56$ g cm^{-3}. Values for ξ[10] = 60° are in Table 2.

4.3.2. 2004 SC$_{60}$

We observed this object with both telescopes from 2019 to 2022. By merging all our data sets of 2004 SC$_{60}$, a long periodicity of 0.083 cycles day^{-1} is found. In Figure 7, we report a fragmented lightcurve with $P^{\rm double}_{\rm rotational} = 58.09 \pm 0.08$ hr with $\Delta m = 0.44 \pm 0.04$ mag (the second maximum of the curve is incomplete, and thus the amplitude can be a bit larger than the one reported here). Once again, the Fourier series fit is unable to reproduce this lightcurve. Due to the fragmentary state of the lightcurve, the presence of the V/U shapes is difficult to evaluate, but the second minimum appears to be sharp. We infer that 2004 SC$_{60}$ is a likely contact binary with

---

[9] A lightcurve is considered asymmetric if its two maxima (and/or both minima) do not reach the same magnitude. In the case of 2001 QF$_{331}$, the two maxima are not reaching the same magnitude, and the two minima are also not at the same magnitude.

[10] Sheppard & Jewitt (2004); Sheppard (2004) showed that an average viewing angle is $\xi = 60°$.

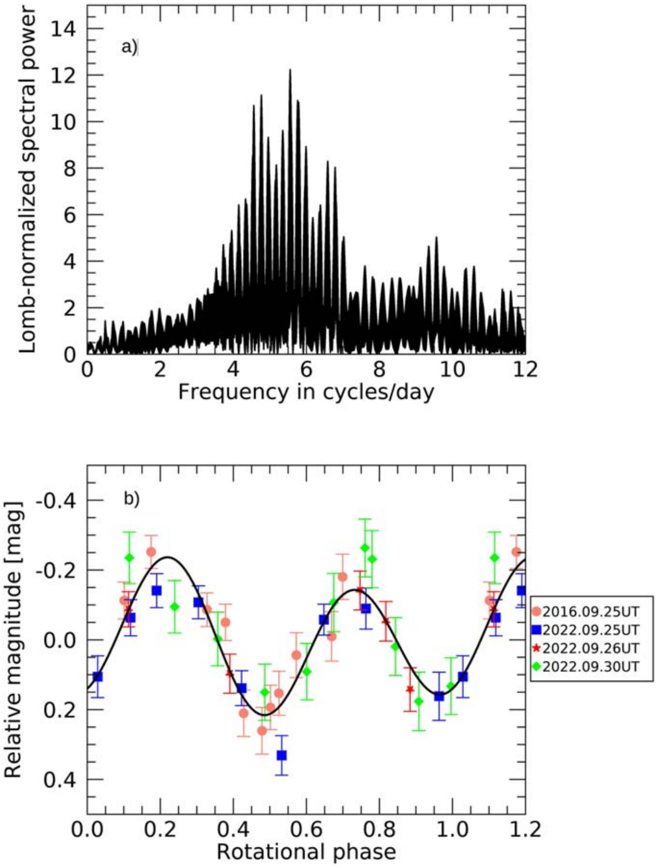

Figure 6. The periodogram's tallest peak is at 5.56 cycles day^{-1}, but as the lightcurve of 2001 QF$_{331}$ is asymmetric and has a large amplitude, the double-peaked period of 8.63 hr is the adequate solution. The lightcurve is fitted with a second-order Fourier series (black curve) suggesting that this object is elongated.

$q_{\min} \sim 0.4$ and $\rho_{\min} \sim 1$ g cm^{-3}. As the amplitude is likely larger than the one reported here, the mass ratio is probably underestimated, and the density is overestimated.

In 2023 October, we estimated that the surface colors of 2004 SC$_{60}$ are very red, with $g' - i' = 1.15 \pm 0.05$ and $g' - r' = 0.83 \pm 0.05$ mag.

4.3.3. 2004 VE$_{131}$

This object was observed five times over 2021. The shortest observing block was 3.5 hr, whereas the longest was about 8 hr, and over most blocks, 2004 VE$_{131}$ displays a large amplitude from ∼0.3 to 0.4 mag (Appendix A and Figure 8). None of our data sets shows a consecutive maximum and minimum over one observing night, and thus we assume that this object rotates very to extremely slowly (probably several days for its period). The fourth and fifth partial lightcurves sample one (or both) of the lightcurve maxima, and they look like U-shaped maxima. Also, the third partial lightcurve is a sharp minimum, which can be a V shape. Therefore, even without enough data to produce the full lightcurve of 2004 VE$_{131}$, we have some hints that this object is of interest, and we propose that it is a potential contact binary. Due to the lack of a full lightcurve, we cannot extract information about the system. No other lightcurve study has been published for this object, so we cannot reaffirm our results. We call for more data to characterize this object/system.

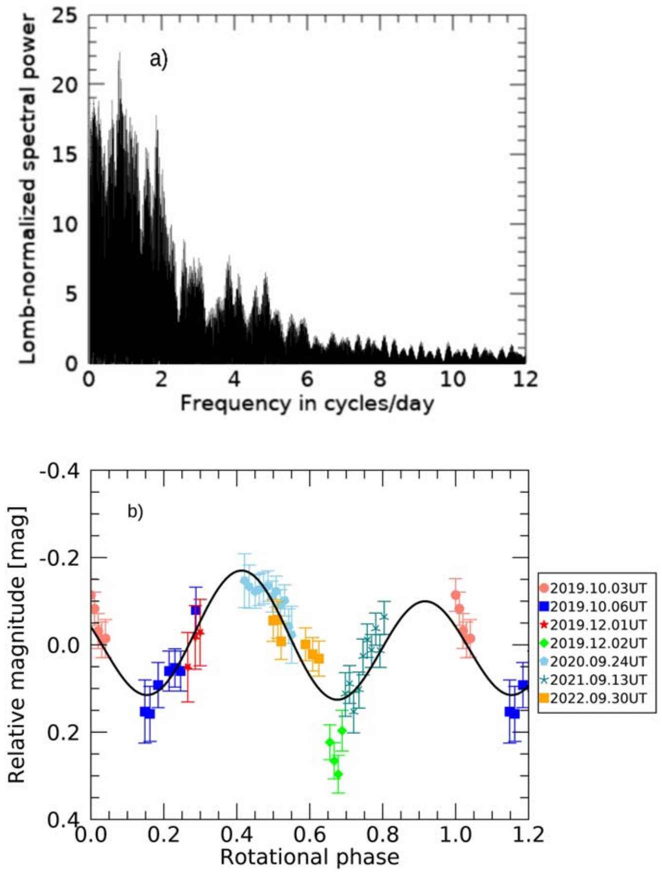

Figure 7. We suggest that 2004 SC$_{60}$ has a double-peaked rotation of 58.09 ± 0.08 hr and $\Delta m = 0.44 \pm 0.04$ mag. The lightcurve morphology is best interpreted if 2004 SC$_{60}$ is a likely contact binary. The χ^2 of the Fourier series fit is 1.65.

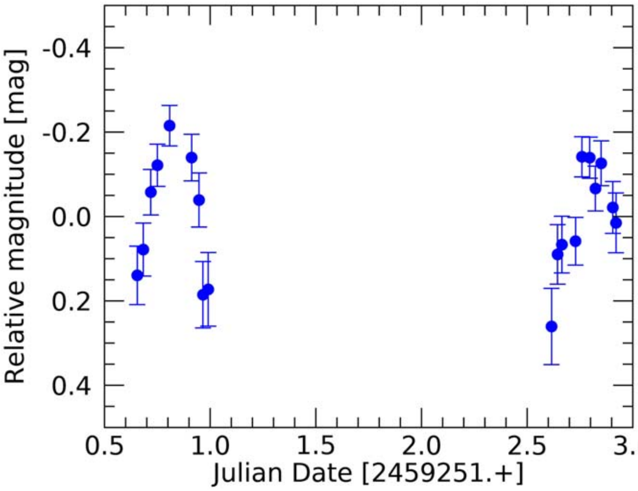

Figure 8. The partial lightcurve of 2004 VE$_{131}$ using only the 2021 December data from the LDT displays a large amplitude and gives us a hint that the lightcurve of this object is asymmetric. 2004 VE$_{131}$ is a potential contact binary.

4.3.4. (434709) 2006 CJ$_{69}$

From 2021 to 2022, we observed 2006 CJ$_{69}$ with the LDT. The tallest peak in Figure 9 is at 2.05 cycles day^{-1}. Because of the large lightcurve amplitude, the double-peaked periodicity

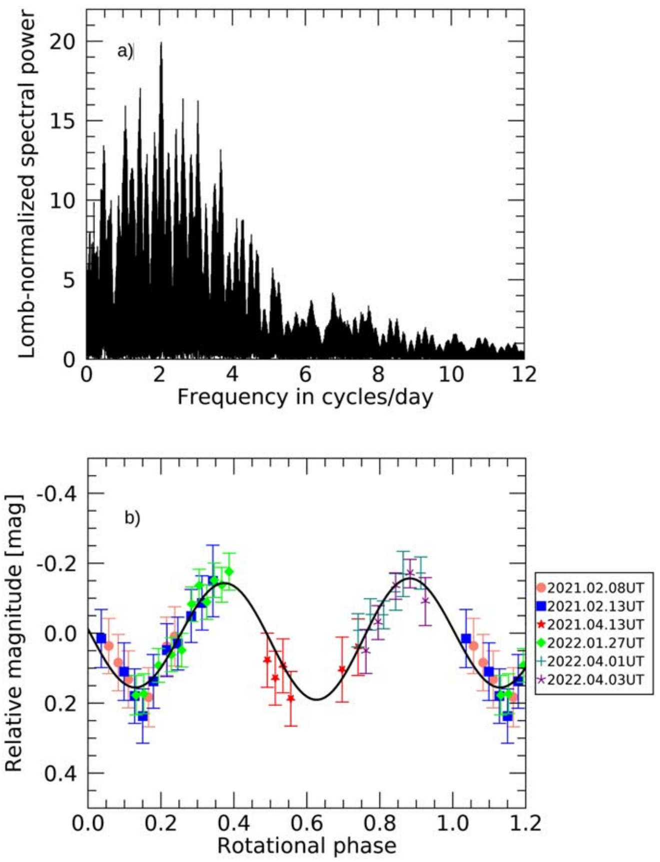

Figure 9. The periodicity of 2006 CJ$_{69}$ is $P_{\rm rotational}^{\rm double} = 23.39 \pm 0.07$ hr (with the periodogram tallest peak at $f = 2.05$ cycles day^{-1}; plot (a)). 2006 CJ$_{69}$ is a likely contact binary, as shown by its variability and nonsinusoidal lightcurve. The χ^2 of the Fourier series fit is 1.19.

with $P_{\rm rotational}^{\rm double} = 23.39 \pm 0.07$ hr seems adequate. The lightcurve amplitude is 0.35 ± 0.04 mag. The overplotted fit shows that the 2006 CJ$_{69}$ lightcurve is not sinusoidal and the minimum is V-shaped. Based on this work, we interpret that 2006 CJ$_{69}$ is a likely contact binary with a mass ratio $q_{\rm min} \sim q_{\rm max} \sim 0.2$ for $\rho_{\rm min}$ = 1 g cm^{-3} or $\rho_{\rm max}$ = 5 g cm^{-3}. Because $\rho_{\rm max}$ is unlikely for a TNO, $\rho_{\rm min}$ is used for our modeling in Table 2.

4.3.5. (531917) 2013 BN$_{82}$

We imaged this object over two years with the LDT. The strongest identified periodicity is 2.63 cycles day^{-1}, but the double-peaked lightcurve with $P_{\rm rotational}^{\rm double} = 18.22 \pm 0.04$ hr is a better match with $\Delta m = 0.40 \pm 0.04$ mag (Figure 10). The Fourier series fit is not a perfect match, but we must point out that the data points forming the lightcurve are a bit sparse. We suggest that 2013 BN$_{82}$ is a likely contact binary, but we caution the reader that more data are required to secure this conclusion.

We model 2013 BN$_{82}$ with a mass ratio of $q_{\rm min} \sim 0.25$ to $q_{\rm max} \sim 0.3$ with a density of $\rho_{\rm min}$ = 1 g cm^{-3} to $\rho_{\rm max}$ = 5 g cm^{-3}. In Table 2, we use a conservative $q = 0.3$ and ρ = 1 g cm^{-3} to derive some basic information about this binary.

Some g', r', i' images infer that 2013 BN$_{82}$ is an ultrared TNO with $g' - i' = 1.31 \pm 0.05$ and $g' - r' = 0.98 \pm 0.05$ mag (Section 5.3).

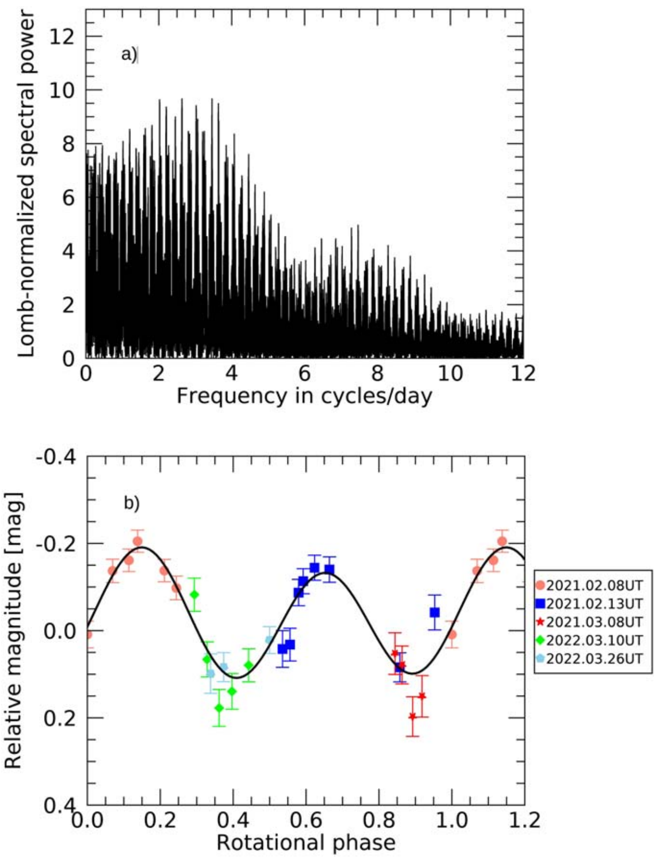

Figure 10. A double-peaked lightcurve with $P_{\rm rotational}^{\rm double} = 18.22 \pm 0.04$ hr and $\Delta m = 0.40 \pm 0.04$ mag is favored for 2013 BN$_{82}$. The fit is not perfect for our data ($\chi^2 = 1.53$), inferring that 2013 BN$_{82}$ is a likely contact binary.

4.3.6. (543734) 2014 OL$_{394}$

In 2016 and 2017, we obtained some images of 2014 OL$_{394}$ over approximately 4 hr in both cases. Its variability is about 0.28 mag in 2016 and about 0.41 mag in 2017. We conclude that 2014 OL$_{394}$ rotates in more than 4 hr with an amplitude higher than 0.41 mag. More observations are warranted to complete this lightcurve because based on its amplitude, 2014 OL$_{394}$ is a potential contact binary.

2014 OL$_{394}$ is an ultrared object with $g' - i' = 1.34 \pm 0.06$ and $g' - r' = 0.87 \pm 0.06$ mag.

4.4. Objects with Δm between 0.2 and 0.3 mag

4.4.1. (523688) 2014 DK$_{143}$

We derive the complete lightcurve of 2014 DK$_{143}$ with one observing night in 2021 May and four in 2023 April. The tallest peak of the periodogram in Figure 11 is at 5.34 cycles day^{-1}. The lightcurve is asymmetric, stating that the double-peaked period of 8.99 ± 0.03 hr is satisfactory with an amplitude of 0.21 ± 0.03 mag. The lightcurve's sinusoidal nature advises that 2014 DK$_{143}$ is a moderately elongated object with $a/b = 1.21$, $c/a = 0.53$, and $\rho > 0.49$ g cm^{-3} if $\xi = 90°$ (Table 2).

In 2023 June, we imaged 2014 DK$_{143}$ with the g', r', i' Sloan filters deriving its colors: $g' - r' = 0.80 \pm 0.03$ and $g' - i' = 1.12 \pm 0.03$ mag. These colors indicate that this object is one of the few moderately red objects trapped in the 5:3 resonance (Section 5.3).

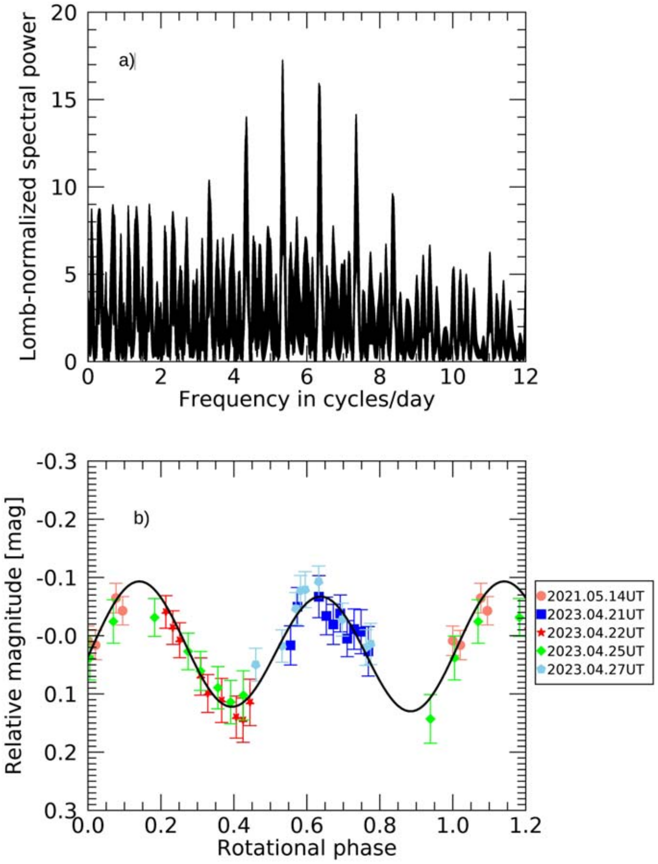

Figure 11. The rotation of 2014 DK$_{143}$ is $P^{\text{double}}_{\text{rotational}} = 8.99 \pm 0.03$ hr. The asymmetric lightcurve with $\Delta m = 0.21 \pm 0.03$ mag is well fitted by a Fourier series demonstrating that this object is elongated and has spot(s) on its surface.

4.4.2. 2014 OQ$_{15}$

The partial lightcurve has $\Delta m \sim 0.28$ mag over about 2 hr.

4.5. Objects with Δm < 0.2 mag

4.5.1. 1999 HG$_{12}$

With one night of observing, the amplitude of 1999 HG$_{12}$ varies by about 0.18 mag in 5 hr.

4.5.2. (129772) 1999 HR$_{11}$

Over two consecutive nights, 1999 HR$_{11}$ has an amplitude of ∼0.17 mag. We constrain its rotational period to be more than 7 hr.

4.5.3. (60620) 2000 FD$_8$

Two observing instances of about 2 hr each show a very low variability of 0.03–0.09 mag.

4.5.4. (469420) 2001 XP$_{254}$

Over approximately 6 hr of observations, the brightness of this TNO decreased by ∼0.12 mag. 2001 XP$_{254}$ was also observed by Kecskeméthy et al. (2023) with the K2 space telescope. They identified two long periodicities (46.719 and 117.157 hr) that we cannot probe with our 6 hr observing block with an amplitude of about 0.28 mag.

4.5.5. (149349) 2002 VA$_{131}$

Over approximately 6 hr, this object's variability is low at about 0.05 mag.

4.5.6. 2002 VV$_{130}$

From three observing blocks of 3, 8, and 3.5 hr, we are unable to retrieve a periodicity and can only conclude that 2002 VV$_{130}$ rotates in more than 8 hr with $\Delta m \sim 0.14$ mag.

4.5.7. (533028) 2014 AL$_{55}$

We observed this object twice, and its variability is ∼0.11 mag in 3 hr.

4.5.8. (523731) 2014 OK$_{394}$

After 4 hr, we conclude that this object has a ∼0.05 mag variability.

4.5.9. (523742) 2014 TZ$_{85}$

Based on an observing run carried out in 2023 February, the variability of 2014 TZ$_{85}$ is only 0.08 mag in ∼4 hr.

4.5.10. (559179) 2015 BR$_{518}$

With images from 2020 over 3.5 hr and about 5 hr in 2021, we suggest that this small body rotates in more than 5 hr with a variability larger than 0.14 mag.

4.5.11. Flat Lightcurves

Five TNOs—(612086) 1999 CX$_{131}$, (385527) 2004 OK$_{14}$, (470523) 2008 CS$_{190}$, 2012 BY$_{154}$, and 2013 SJ$_{102}$—have such an extremely low variability that their lightcurves are flat over the observing time per target. The causes of a flat lightcurve are a spheroidal small body with a homogeneous surface, a slow rotator with a period longer than the time spanned imaging the object, and/or a pole-on orientation. Based on Kepler 2 data obtained over ∼38 days, Kecskeméthy et al. (2023) also conclude that the variability of 2008 CS$_{190}$ is extremely low, with $\Delta m < 0.022$ mag and no retrievable period.

5. Discussion

5.1. Our Survey and the Literature

Prior to our survey, only four 5:3 and three 7:4 resonant TNOs had some published short-term variability information (Figure 1 and Table 3). Our survey increases by more than 300% the number of short-term studies of resonant TNOs. Alongside targeting TNOs brighter than ∼24 mag, selected TNOs have a mixture of absolute magnitudes and orbital elements to probe differences (if any) within the populations.

The histograms in Figure 13 present the amplitude distributions of both resonances (and 2003 SP$_{317}$) by mixing our survey and the literature. Lightcurve amplitude ranges from flat to about 1 mag, but only ∼21% have no noticeable variability. Overall, both resonances have objects with variability up to 0.6 mag, with the exception of 2013 FR$_{28}$ and 2003 SP$_{317}$, whose amplitudes are 0.85 and 0.94 mag. The entire sample average amplitude is 0.47 mag for the full lightcurve. Complete lightcurves in the 5:3/7:4 resonances have an average of 0.34/0.52 mag, while the partial lightcurves have an average of 0.20/0.19 mag. The average amplitude in the 5:3 is consistent

Table 3
Published Photometric Studies of 5:3 and 7:4 Resonant TNOs

Object	$P_{\text{rotational}}^{\text{single}}$ (hr)	$P_{\text{rotational}}^{\text{double}}$ (hr)	Δm (mag)	H_{MPC} (mag)	Reference[a]	Wide Binary[b] (yes/no/?)
			Mean-motion Resonance: 5:3			
(126154) 2001 YH$_{140}$[c]	6.22/8.45 ± 0.05/12.99	⋯	0.19 ± 0.14	5.58	O06	No
	13.25 ± 0.2	⋯	0.21 ± 0.04	⋯	S07	⋯
	13.19	⋯	0.13 ± 0.05	⋯	T10, T13	...
	13.705 ± 0.039	27.397 ± 0.172	0.095/0.229 ± 0.019	⋯	K23	...
(469420) 2001 XP$_{254}$	46.719 ± 0.422	⋯	0.282 ± 0.056	7.78	K23	Yes
	117.157 ± 2.328	⋯	0.275 ± 0.056	⋯	K23	⋯
(470523) 2008 CS$_{190}$			<0.022	6.27	K23	No
2015 RJ$_{278}$	⋯	⋯	<0.10	7.7	A19	?
			Mean-motion Resonance: 7:4			
(119066) 2001 KJ$_{76}$[d]	3.38 ± 0.39	⋯	0.34 ± 0.06	6.52	K06	?
(385446) 2003 QW$_{111}$ Manwë–Thorondor[e]	⋯	11.926 78 ± 0.0007	0.48 ± 0.01	6.57	R20	Yes
2013 UK$_{17}$	⋯	⋯	<0.10	6.8	A19	?

Notes. The 7:4 resonant/classical (https://www.boulder.swri.edu/buie/kbo/astrom/160147.html) TNO named (160147) 2001 KN$_{76}$ was observed by Kern (2006). Unfortunately, the lightcurve (and the photometry of each image) is unavailable, so we cannot assess the lightcurve quality. For the purpose of this work, we exclude the results from Kern (2006) about 2001 KN$_{76}$. 2015 RE$_{278}$ is classified as a 7:4 resonant TNO by Alexandersen et al. (2019) but as a classical TNO according to the DES (https://www.boulder.swri.edu/buie/kbo/astrom/15RE278.html). Because of an ambiguous classification, this TNO has been excluded from our analysis.

[a] References are K06: Kern (2006), O06: Ortiz et al. (2006), S07: Sheppard (2007), T10: Thirouin et al. (2010), T13: Thirouin (2013), A19: Alexandersen et al. (2019), R20: Rabinowitz et al. (2020), K23: Kecskeméthy et al. (2023).

[b] Known resolved binaries are listed with a "yes," single objects without a satellite detected by the HST have a "no," and objects never observed by HST (and so with an unknown resolved binary nature) have a "?." The same definition has been applied in Table 1. Objects in this table were imaged by HST programs 11113 and 12468 (K. S. Noll et al.) and 11178 and 13404 (W. M. Grundy et al.).

[c] Based on a data set from 2004 December, Ortiz et al. (2006) favored a single peak of 8.45 hr for 2001 YH$_{140}$ but also discussed two potential aliases at 6.22 and 12.99 hr. Thirouin et al. (2010) reanalyzed the Ortiz et al. (2006) data set and favored a rotation of 13.19 hr, which is in agreement with the periodicity obtained by Sheppard (2007) based on an independent data set from 2003 December. By merging the data sets from Sheppard (2007) and Thirouin et al. (2010), Thirouin (2013) favored a rotational period of 13.19 hr. Kecskeméthy et al. (2023) found a similar single-peaked periodicity of about 13 hr, but they favored the double-peaked solution. We favor the single-peaked lightcurve for this paper.

[d] The single-peaked lightcurve of 2001 KJ$_{76}$ reported by Kern (2006) has a rotational period of 3.38 hr. Due to the large amplitude and the TNO spin barrier at ∼4 hr, the double-peaked periodicity (i.e., 6.76 hr) seems more appropriate and will be used for this paper (Thirouin et al. 2010, 2014). However, Kern (2006) is based on only six images; therefore, we emphasize that the periodicity and amplitude are highly uncertain.

[e] (385446) 2003 QW$_{111}$ is a resolved binary system whose primary is Manwë and companion is Thorondor (Noll et al. 2006). Grundy et al. (2014) predicted that the system would have a mutual event season in 2015–2017. Based on Rabinowitz et al. (2020), the system's mutual event season is explainable if Manwë is a contact binary and Thorondor is highly elongated.

with the one in the cold classical population (Thirouin & Sheppard 2019a). Bodies in the 7:4 have larger variabilities than the cold classicals, whose high variability was demonstrated by Thirouin & Sheppard (2019a).

In the following, we aim to compare the rotational frequency distributions of the objects studied in this paper to the most likely/likely close/contact binaries as well as to the dynamically cold classical population and ultimately to the other TNOs (Figure 12). As in Binzel et al. (1989), we use a Maxwellian fit to match the rotational frequency distribution of these objects (Figure 12). The fit gives a mean period[11] of $P_{\text{Maxwellian}}^{\text{mean}} = 10.67 \pm 1.93$ hr. This mean rotational period indicates that the resonant TNOs within the classical belt rotate slowly in comparison to the other TNOs ($P_{\text{Maxwellian}}^{\text{mean}} = 8.74 \pm 0.66$ hr) and even potentially slower than the dynamically cold classicals ($P_{\text{Maxwellian}}^{\text{mean}} = 10.74 \pm 1.47$ hr) whose slow rotation was pointed out by Thirouin & Sheppard (2019a). However, the mean period uncertainties derived from the fits are large, and thus we infer that both the resonant and cold classical TNOs have long rotations.

The bubble plot in Figure 13 regroups the TNOs with partial and full lightcurves, while the point size indicates the object's

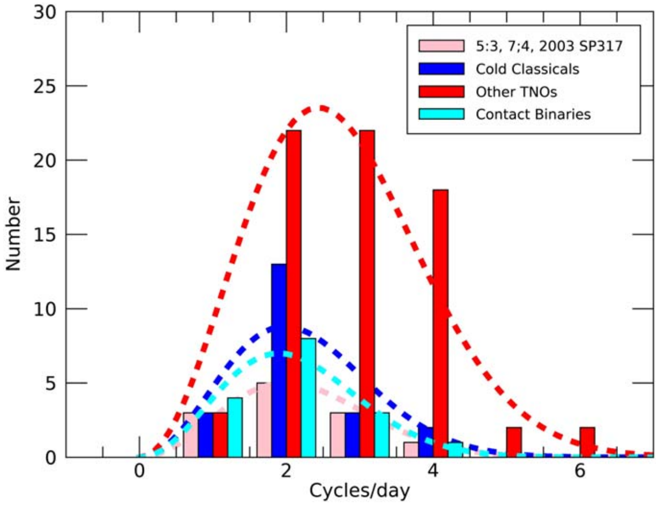

Figure 12. We overplot a Maxwellian distribution to fit the rotational frequency distribution of several subpopulations, such as the cold classicals, the contact binaries across the trans-Neptunian belt, the other TNOs including all the objects except for the cold classicals and the resolved binaries, and the TNOs discussed in this paper. All the subpopulations follow a Maxwellian distribution, and we infer that the mean rotational periods of the cold classicals and TNOs from this paper are similar.

---

[11] If 2003 SP$_{317}$ is not considered, $P_{\text{Maxwellian}}^{\text{mean}} = 10.50 \pm 1.98$ hr.

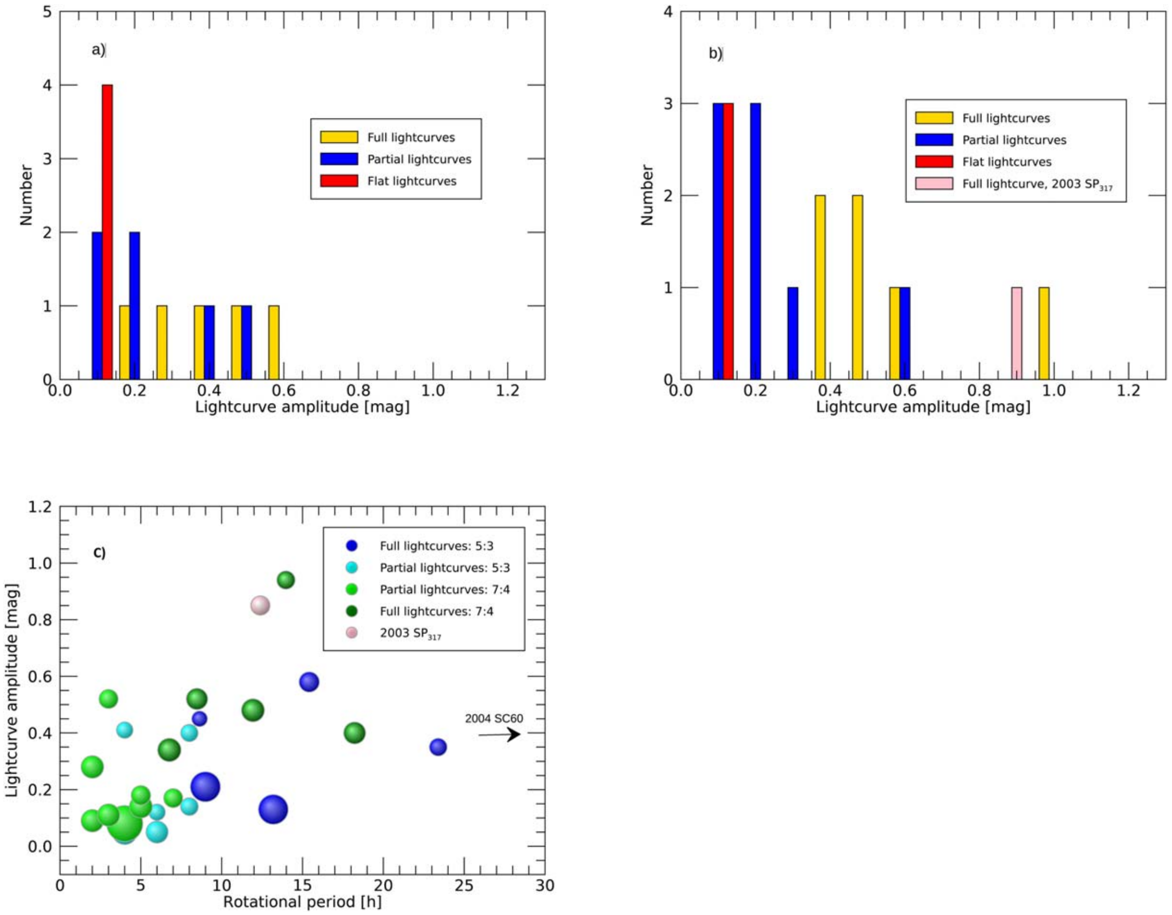

Figure 13. The amplitude distributions for the 5:3 and 7:4 resonances are plotted (plots (a) and (b)). Due to the ambiguous dynamical class of 2003 SP$_{317}$, it is color-coded differently and added to the distribution of the 7:4 being the closest in semimajor axis. Only ∼23% have a flat lightcurve. Similarly, as for the cold classicals, there is a trend between amplitude and period (plot (c); Thirouin & Sheppard 2019a).

size. By looking at this plot, we can see a trend between period and amplitude with the slowest rotators having the highest variability. To confirm such a trend and find others, we run a correlation search using the program `ASURV`, which allows data sets with upper and/or lower limits (Spearman 1904; Isobe et al. 1986). (Anti)correlations are in Table 4. As suggested by the bubble plot, there is a strong correlation between amplitude and period with a Spearman value of 0.537 at a significance level of 99% for the combined 5:3, 7:4, and 2003 SP$_{317}$. By probing only the 5:3 and 7:4 resonances, this tendency is also present, but it is stronger in the 7:4 resonance. This trend is also present in the dynamically cold classicals (Thirouin & Sheppard 2019a). The usual relation with amplitude and absolute magnitude (high amplitude at small size) that has been already identified in numerous studies is also found in our groupings (e.g., Sheppard et al. 2008; Benecchi & Sheppard 2013; Thirouin et al. 2016; Thirouin & Sheppard 2019a; Alexandersen et al. 2019). In the 5:3 resonance, small bodies with higher variabilities are at low inclinations, and slow rotators are at lower eccentricities. In the 7:4, slow rotators are at low inclinations and high eccentricities. The complete lightcurves favor high amplitudes at low inclinations. As we will discuss in Section 5.3, low inclinations are dominated by cold classical TNOs in these resonances, and as demonstrated by Thirouin & Sheppard (2019a), the cold classicals are slow rotators with a higher amplitude compared to the other trans-Neptunian populations. With low significance levels, it is possible that small objects rotate slowly in the 7:4 resonance as well as based on the complete lightcurve sample. Similarities with the dynamically cold classicals and other resonant populations will be debated in Section 5.4.

5.2. Contact Binaries

In Section 4, we report that 2013 FR$_{28}$ is a most likely contact binary, while 2003 SP$_{317}$, 2004 SC$_{60}$, 2006 CJ$_{69}$, and 2013 BN$_{82}$ are likely contact binaries, and we also classify 1999 HT$_{11}$, 2004 VE$_{131}$, and 2014 OL$_{394}$ as potential contact binaries due to their variabilities. Rabinowitz et al. (2020) suggest that the primary of Manwë–Thorondor is a contact binary. Because the lightcurve of Manwë–Thorondor is below the 0.9 mag limit and for consistency in this paper, we consider Manwë–Thorondor as a likely contact binary. In total, nine objects are showing signs of contact binarity.

The range of variability for the contact binaries infers a diversity of the system's geometries and characteristics (Table 2). All contact binary candidates have a moderate eccentricity with $e > 0.2$ and a low inclination with $i < 10°$, except for 2006 CJ$_{69}$, whose inclination is 17°.9, as well Manwë–Thorondor and 1999 HT$_{11}$, whose eccentricities are $e < 0.2$. Out of all the contact binaries discovered with the lightcurve and occultation techniques, most of them have an inclination lower than 10° (Thirouin & Sheppard 2019b; Buie et al. 2020; Leiva et al. 2020, 2023). In this paper, contact binaries are small TNOs with absolute magnitude $H > 7.2$ mag,

Table 4
(Anti)correlation for the 5:3 and 7:4 Resonances and 2003 SP$_{317}$

Values	Spearman Coefficient	Significance Level (%)
All Objects, $\#_{\text{total}} = 26$		
Amplitude/semimajor axis	0.110	42
Amplitude/absolute magnitude	0.322	89
Amplitude/inclination	−0.307	87
Amplitude/eccentricity	0.077	30
Amplitude/ascending node	−0.045	18
Amplitude/argument of perihelion	−0.352	92
Amplitude/perihelion distance	0.011	4
Amplitude/aphelion distance	0.249	79
Amplitude/period	0.537	99
Period/semimajor axis	−0.173	61
Period/absolute magnitude	0.247	78
Period/inclination	−0.167	60
Period/eccentricity	0.203	69
Period/ascending node	0.198	68
Period/argument of perihelion	−0.138	51
Period/perihelion distance	−0.219	73
Period/aphelion distance	0.134	50
5:3 Resonants, $\#_{\text{total}} = 11$		
Amplitude/semimajor axis	0.067	17
Amplitude/absolute magnitude	0.302	66
Amplitude/inclination	−0.687	97
Amplitude/eccentricity	0.168	40
Amplitude/ascending node	0.021	5
Amplitude/argument of perihelion	−0.459	85
Amplitude/perihelion distance	−0.177	42
Amplitude/aphelion distance	0.168	40
Amplitude/period	0.405	81
Period/semimajor axis	−0.763	98
Period/absolute magnitude	−0.202	48
Period/inclination	0.302	66
Period/eccentricity	−0.241	55
Period/ascending node	−0.329	70
Period/argument of perihelion	−0.406	80
Period/perihelion distance	0.201	47
Period/aphelion distance	−0.241	55
7:4 Resonants, $\#_{\text{total}} = 14$		
Amplitude/semimajor axis	−0.361	81
Amplitude/absolute magnitude	0.588	97
Amplitude/inclination	−0.130	36
Amplitude/eccentricity	0.139	38
Amplitude/ascending node	−0.213	56
Amplitude/argument of perihelion	−0.293	71
Amplitude/perihelion distance	−0.163	44
Amplitude/aphelion distance	0.176	47
Amplitude/period	0.595	97
Period/semimajor axis	0.105	29
Period/absolute magnitude	0.409	86
Period/inclination	−0.443	89
Period/eccentricity	0.476	91
Period/ascending node	0.450	90
Period/argument of perihelion	−0.036	10
Period/perihelion distance	−0.477	91
Period/aphelion distance	0.475	91
Complete Lightcurves, $\#_{\text{total}} = 12$		
Amplitude/semimajor axis	0.294	67
Amplitude/absolute magnitude	0.557	94
Amplitude/inclination	−0.587	95
Amplitude/eccentricity	0.301	68
Amplitude/ascending node	−0.112	29
Amplitude/argument of perihelion	−0.636	97
Amplitude/perihelion distance	−0.112	29
Amplitude/aphelion distance	0.545	93
Amplitude/period	0.056	15
Period/semimajor axis	−0.126	32
Period/absolute magnitude	0.343	75
Period/inclination	−0.203	50
Period/eccentricity	0.413	83
Period/ascending node	0.329	72
Period/argument of perihelion	−0.154	39
Period/perihelion distance	−0.385	80
Period/aphelion distance	0.280	65

Note. All trends from very strong to nonexistent are reported in this table. A trend is strong if the absolute value of the Spearman coefficient is larger than 0.3. If the absolute value is higher than 0.6, the trend is very strong, and if the absolute value is less than 0.3, there is no trend. Trends with ascending node, aphelion, and perihelion distance are likely due to observational biases. If the significance level is higher than 99%, the trend is very strong, but if the significance level is higher than 97.5%/95%, the trend is strong/reasonably strong. See Spearman (1904) for more details.

aside from 2013 BN$_{82}$, whose absolute magnitude is 6.73 mag. Similarly, in the 3:2 and 2:1 resonances, contact binaries have $H > 7$ mag, but they are bigger in the cold classical dynamical group (Thirouin & Sheppard 2018, 2019a, 2022).

With a complete sample composed of our survey and the literature, the lower estimate of the fraction of nearly equal-sized contact binaries in several object groupings can be estimated. Thirouin & Sheppard (2022) summarize the approach, and here we follow it to derive fractions based on Equation (1) ($f^{\text{Eq.1}}$) and Equation (2) ($f^{\text{Eq.2}}$). As already mentioned in Sheppard & Jewitt (2004) and Thirouin & Sheppard (2022), Equation (1) assumes objects with axes such as $a > b$ and $b = c$, whereas Equation (2) considers triaxial objects with $a \geqslant b = c$. We list our fraction estimates in Table 5. In the first step, only the amplitude, and not our interpretation in Section 4, has been considered. As an

Table 5
Contact Binary Fractions in Several Object Groupings and with Different Magnitude Cutoffs

Sample	Δm^{cut} (mag)	No.	$f^{\text{Eq.1}}$ (%)	$f^{\text{Eq.2}}$ (%)
All Objects, $\#_{\text{total}} = 15$				
5:3	$\geqslant 0.9$	0	0	0
	$\geqslant 0.5$	1	~ 11	~ 12
	$\geqslant 0.4$	4	~ 36	~ 42
	$\geqslant 0.3$	5	~ 38	~ 46
All Objects, $\#_{\text{total}} = 17$				
7:4	$\geqslant 0.9$	1	~ 35	~ 20
	$\geqslant 0.5$	3	~ 30	~ 31
	$\geqslant 0.4$[a]	6	~ 47	~ 55
All Objects, $\#_{\text{total}} = 33$				
5:3, 7:4, 2003 SP_{317}	$\geqslant 0.9$	1	~ 18	~ 10
	$\geqslant 0.8$	2	~ 23	~ 17
	$\geqslant 0.5$	4	~ 26	~ 27
	$\geqslant 0.4$	10	~ 44	~ 52
	$\geqslant 0.3$	11	~ 42	~ 51
All Objects minus Elongated Ones, $\#_{\text{total}} = 15$				
5:3	$\geqslant 0.4$	2	~ 18	~ 21
	$\geqslant 0.3$	3	~ 23	~ 28
All Objects minus Elongated Ones, $\#_{\text{total}} = 17$				
7:4	$\geqslant 0.9$	1	~ 35	~ 20
	$\geqslant 0.5$	2	~ 20	~ 21
	$\geqslant 0.4$	5	~ 39	~ 46
All Objects minus Elongated Ones, $\#_{\text{total}} = 33$				
5:3, 7:4, 2003 SP_{317}	$\geqslant 0.9$	1	~ 18	~ 10
	$\geqslant 0.8$	2	~ 23	~ 17
	$\geqslant 0.5$	3	~ 15	~ 16
	$\geqslant 0.4$	8	~ 32	~ 38
	$\geqslant 0.3$	9	~ 31	~ 38

Note.
[a] Only one 7:4 resonant object, 2001 KJ_{76}, has an amplitude between 0.3 and 0.4 mag, but as its lightcurve is uncertain, we do not consider the cutoff at 0.3 mag for the 7:4 resonance.

example, in the 7:4 resonance, lightcurve information is known for 17 TNOs, and there are six objects with $\Delta m \geqslant 0.4$ mag, which gives $f^{\text{Eq.1}} \sim 47\%$ and $f^{\text{Eq.2}} \sim 55\%$. But one of these five objects is 2015 FP_{345}, which we have classified as an elongated object. So, our second step is to consider the amplitude cutoff and our interpretation, and in such a case, the 7:4 resonance has five nonelongated objects with $\Delta m \geqslant 0.4$ mag, which gives $f^{\text{Eq.1}} \sim 39\%$ and $f^{\text{Eq.2}} \sim 46\%$.

Based on the different values reported in Table 5, we conclude that the 5:3 resonance has a lower estimate of ~10%–50% of (nearly) equal-sized contact binaries, while the 7:4 resonance has a percentage of ~20%–55%, and the full sample infers a fraction of ~10%–50%. In conclusion, both resonances have about the same fraction of contact binaries. Overall, the fractions overlap with the predicted one by Nesvorný & Vokrouhlický (2019) at 10%–30%.

Though there is overlap in the expected fraction of nearly equal-sized contact binaries in the 5:3, 7:4, and cold classical regions, in general, it appears the 5:3 and 7:4 resonances have more contact binaries than the cold classicals (Thirouin & Sheppard 2019a). If further observations continue to show that the number of contact binaries in the cold classical belt is lower than in the resonances, it is possible that contact binaries are preferentially formed when objects are gravitationally perturbed while they escape the cold classical population or once they are trapped into the resonances (Thirouin & Sheppard 2019a, 2019b; Nesvorný & Vokrouhlický 2019).

5.2.1. Contact Binaries with/without a Moon

Both Manwë–Thorondor and 2003 SP_{317} have been imaged with the Hubble Space Telescope (HST) to search for moon(s) around them. No moon was detected for 2003 SP_{317}, but the resolved satellite Thorondor was found around Manwë. Other contact binaries in our sample have never been searched for (widely) separated moon(s) (Table 1). The number of resolved wide binaries in both resonances is low, with only two binaries out of 19 observed TNOs ((385446) Manwë–Thorondor and (525816) 2005 SF_{278}) in the 7:4 and one ((469420) 2001 XP_{254}) out of 13 in the 5:3 resonance (W. M. Grundy, private communication). With ~8% and ~11% of resolved binaries in the 5:3 and 7:4 resonances, respectively, contact binaries seem to be the favored kind of binaries.

5.2.2. Rotation Periods of Contact Binaries

The rotational periods of the most likely/likely contact binaries are from ~6 to ~60 hr, but most have periods between 10 and 20 hr (Sheppard & Jewitt 2004; Lacerda 2011; Lacerda et al. 2014b; Thirouin & Sheppard 2017, 2018, 2019a, 2022; Thirouin et al. 2017; Rabinowitz et al. 2020, and this work). Using the 17 likely/most likely contact binaries with a complete lightcurve, we fit a Maxwellian distribution with $P^{\text{mean}}_{\text{Maxwellian}} = 11.21 \pm 1.76$ hr (Figure 12). This mean period is similar to that of the resolved binary population (10.11 ± 1.19 hr) derived by Thirouin et al. (2014) inferring that resolved and contact binaries are on average slower rotators than the more general trans-Neptunian population. Using numerical simulations including Kozai effects, tidal friction, and giant planets' perturbations on a synthetic population, Brunini (2023) is able to reproduce the excess of contact binaries in the 3:2 (Plutino) resonance. One interesting outcome of the modeling is the rotational period of the 3:2 contact binaries (Figure 4 of Brunini 2023). Even if this distribution is only for the 3:2 TNOs, we note some similarities with the period distribution of all contact binaries (i.e., in all subpopulations), with 76% of contact binaries with a periodicity less than 20 hr, 18% with periods between 20 and 40 hr, and 6% with periods longer than 40 hr.

5.3. Colors

Sheppard (2012) conducted a comprehensive color survey of resonant TNOs, including the two (7:4 and 5:3) resonances targeted in this work. He concluded that the 5:3 and 7:4 resonances, especially at low inclinations, are dominated by ultrared material, which is common for the dynamically cold classical TNOs, while a handful of non-ultrared objects were identified at higher inclinations ($i > 10°$). Sheppard (2012) suggested that these resonances have a low-inclination cold classical component dominated by cold classical TNOs that are now trapped in these resonances, whereas the objects at higher inclination are likely from the dynamically hot classical population. In Figure 14, we plot all the published[12] colors of 5:3 and 7:4 resonants as well as colors from this work

---

[12] We updated the data sets from Sheppard (2012) as some observed objects are not classified as resonant TNOs anymore.

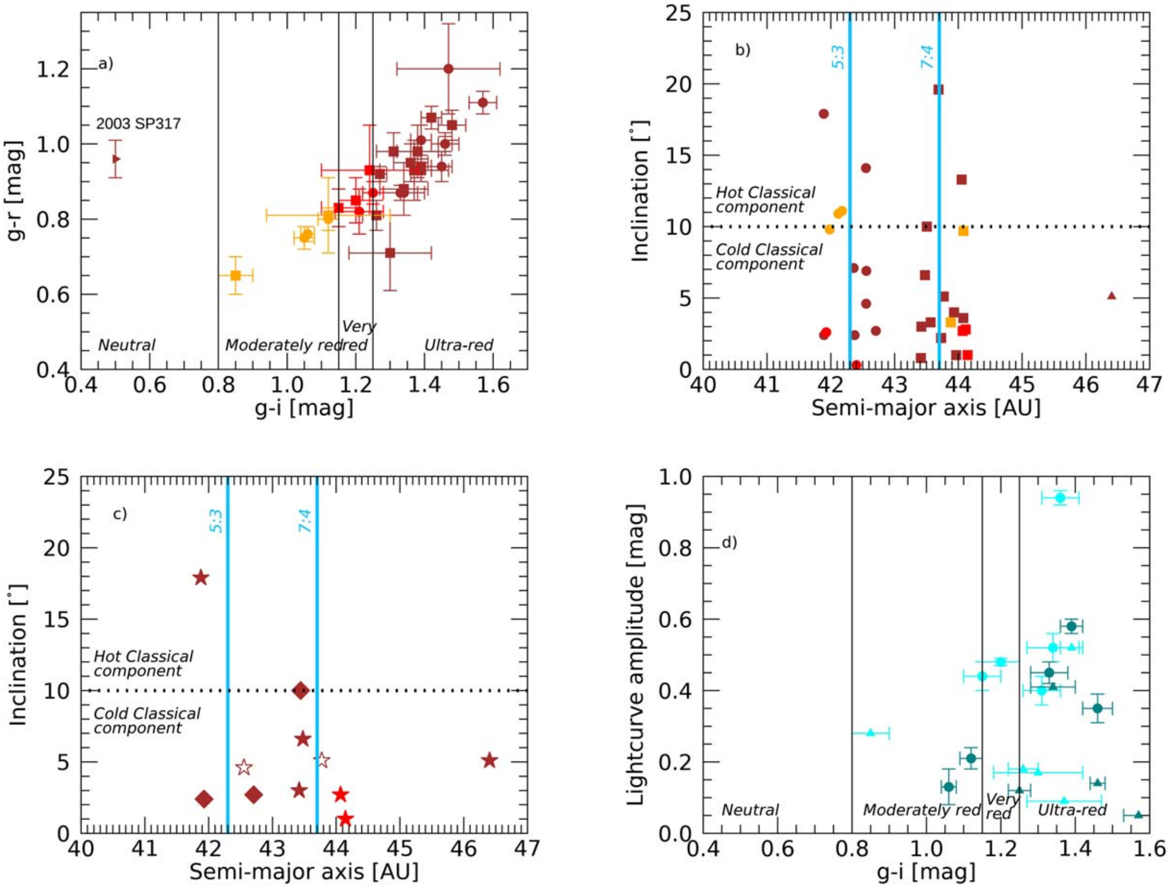

Figure 14. Surface colors of small bodies trapped in the 5:3 (circles) and 7:4 (squares) resonances are color-coded such as orange for moderately red, red for very red, and brown for ultrared surfaces (plots (a) and (b)). The limit at an inclination of 10° separating the cold from the hot classical component is the dotted line (Sheppard 2012). Contact binaries (filled stars for most likely and likely, open stars for potential) and elongated objects (diamonds) are ultrared objects, except Manwë–Thorondor (plot (c)). In plot (d), cyan and teal circles are for 7:4 and 5:3 resonants (respectively) with a full lightcurve, whereas the triangles indicate a lower limit for the lightcurve amplitude. The i'-band magnitude of 2003 SP$_{317}$ (brown triangle in plots (a) and (b)) is unknown; therefore, this object is not included in plot (d), and only the $g' - r'$ is taken into account in plot (a).

Table 6

Colors of Likely/Most Likely Contact Binaries and Elongated Objects

Small Body	$g' - r'$ (mag)	$g' - i'$ (mag)	References
	Likely and Most Likely Contact Binaries		
1999 HT$_{11}$	0.94 ± 0.04	1.39 ± 0.03	Sheppard (2012)
2003 QW$_{111}$	0.85 ± 0.06	1.20 ± 0.05	Sheppard (2012)
2003 SP$_{317}$	0.96 ± 0.05	⋯	Pike et al. (2023)
2004 SC$_{60}$	0.83 ± 0.05	1.15 ± 0.05	This work
2006 CJ$_{69}$	1.00 ± 0.03	1.46 ± 0.04	Sheppard (2012)
2013 BN$_{82}$	0.98 ± 0.05	1.31 ± 0.05	This work
2013 FR$_{28}$	0.95 ± 0.05	1.36 ± 0.05	Thirouin & Sheppard (2019b)
2014 OL$_{394}$	0.87 ± 0.06	1.34 ± 0.06	This work
	Elongated Objects		
2001 QF$_{331}$	0.87 ± 0.02	1.33 ± 0.05	Pike et al. (2017)
2003 YW$_{179}$	1.01 ± 0.04	1.39 ± 0.03	Sheppard (2012)
2015 FP$_{345}$	0.88 ± 0.07	1.34 ± 0.07	This work

(Sheppard 2012; Peixinho et al. 2015; Pike et al. 2017; Thirouin & Sheppard 2019b).

Table 6 summarizes the $g'r'i'$ colors[13] of the contact binaries and elongated objects (with $\Delta m > 0.3$ mag) in the 5:3 and 7:4 resonances as well as 2003 SP$_{317}$. With the exception of 2003 QW$_{111}$ (aka Manwë–Thorondor) and 2004 SC$_{60}$, whose surfaces are still very red, all the contact binaries and elongated objects have an ultrared surface. This color suggests that their origins are in the dynamically cold classical population, which is reinforced by the fact that nearly all these objects have inclinations $i \leqslant 10°$. The only anomaly is the ultrared likely contact binary 2006 CJ$_{69}$ with $i = 17.^{\circ}9$ (Figure 14). But, as demonstrated by Lykawka & Mukai (2005) and Volk & Malhotra (2011), resonant TNOs can be excited to higher inclinations than their original ones. Therefore, the dynamically cold classical population may create a cold classical component in the resonances, but some objects trapped in the resonances may also be dynamically excited to higher inclinations from initially lower inclinations. Also, as illustrated in Figure 14, objects with larger lightcurve amplitudes tend to have high $g' - i'$ colors, demonstrating that TNOs with an origin in the cold classical belt are more deformed/elongated (Thirouin & Sheppard 2019a).

5.4. Resonant versus Cold Classical TNOs

In the following, we compare the rotational properties of the TNOs trapped in several resonances and the cold classicals. The lightcurve survey published in Thirouin & Sheppard (2018, 2019a, 2022), updated with newly published lightcurves

---

[13] Colors of 2014 DK$_{143}$ are not included in Table 6 because this object has a moderate lightcurve amplitude.

(e.g., Alexandersen et al. 2019; Kecskeméthy et al. 2023), is considered.

Kecskeméthy et al. (2023) report the photometry of 66 TNOs in several subpopulations using Kepler 2 data, and by taking advantage of the long and continuous observing blocks, they retrieve long periodicities that are difficult from the ground because they require an extremely large amount of telescope time. Lightcurves from Kecskeméthy et al. (2023) are smoothed lightcurves. Assuming that they followed the methodology in Pál et al. (2015), we speculate that they have weighted the means of the photometry within a box with a certain number of points. Pál et al. (2015) used a box of 68 points to derive a weighted mean magnitude and construct the entire smoothed (or binned) lightcurve. Because there is no detail in Kecskeméthy et al. (2023), we do not know if the same number of points per box was used nor if several numbers of points per box were tested to see if it significantly affects the smoothed lightcurve. In some occurrences, Kecskeméthy et al. (2023) confirm rotational periods and amplitudes derived with ground-based lightcurves, but sometimes the results are quite different. As an illustration, 2014 JQ_{80} is a likely contact binary with a period of 12.16 hr and a variability of 0.76 mag based on a ground-based lightcurve obtained by Thirouin & Sheppard (2018). Kecskeméthy et al. (2023) retrieve a consistent period but an amplitude of only 0.39 mag. Data from Thirouin & Sheppard (2018) are from 2017 May–June, and 2017 September–October for Kecskeméthy et al. (2023); therefore, there is no reason to expect a drastic change of the system's geometry (and so amplitude change) over about five months. Kecskeméthy et al. (2023) argue that the inconsistent amplitudes have to be expected because the object is faint and because of the achievable Kepler 2 accuracy. However, the mean Kepler 2 magnitude of 2014 JQ_{80} is ~22.2 mag, and thus it is not one of the faintest TNOs in their sample.

In Kecskeméthy et al. (2023), the lightcurves of two cold classicals, 2003 YS_{179} and (420356) 2012 BX_{85} Praamzius,[14] catch our attention because of their extreme variabilities of 1.278 ± 0.197 and 1.433 ± 0.181 mag, respectively. If these estimates are correct, these two small bodies would have the largest variability ever recorded in the trans-Neptunian belt. Unfortunately, the authors do not discuss, interpret, or even flag the amplitudes of these objects. Such large variabilities can only be caused by contact binaries, but the smoothed lightcurves do not have U/V shapes. Also, the individual Kepler 2 data are scattered over nearly 6 mag for Praamzius and about 3 mag for 2003 YS_{179}. With mean Kepler 2 magnitudes around 22.5 and 22 mag for 2003 YS_{179} and Praamzius, respectively, they are in the same range as 2014 JQ_{80}. As the authors expressed their concerns regarding the 2014 JQ_{80} results, we can speculate that the same concerns can be expressed for 2003 YS_{179} and Praamzius. In the following, results from Kecskeméthy et al. (2023) are not included in our analysis, as their paper presents some debatable results.

In Figure 15, all 3:2, 5:3, 7:4, and 2:1 resonant TNOs, as well as cold classicals with some rotational information, are plotted. Circles highlight objects with a complete lightcurve, while triangles indicate limits for the period and amplitude. Most of the observed TNOs have an absolute magnitude from 5 to 9 mag. Running means (solid lines in Figure 15) indicate that the amplitude increases at higher absolute magnitudes for all groups with a significant increase starting at $H \sim 6$–7 mag based on the full and partial lightcurves (flat ones are not included). We run a 2D Kolmogorov–Smirnov (K-S) test as implemented in Press et al. (1992) to check if a specific subpopulation is significantly different from another using only the full lightcurves. The test returns two parameters: D, which

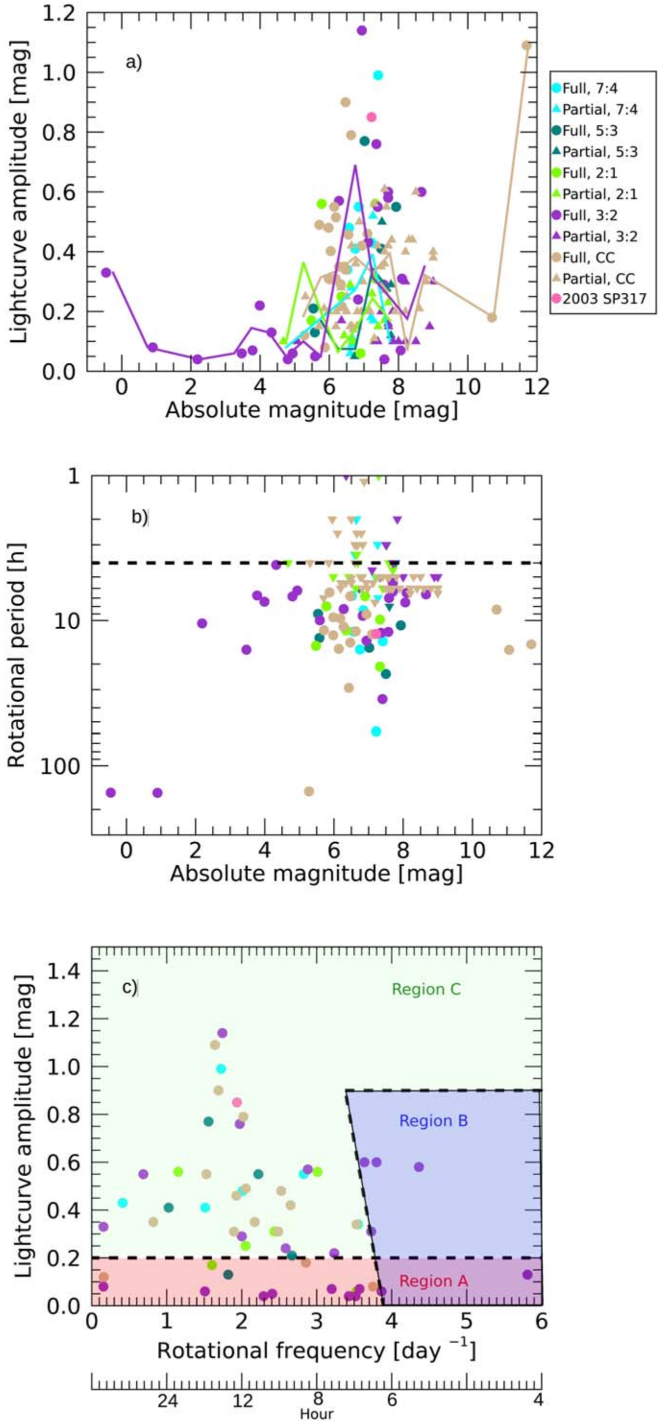

Figure 15. We compare the rotational properties of the 2:1, 3:2, 7:4, 5:3, and cold classical (CC) TNOs (plots (a), (b), and (c)). The legend is the same for all plots. Running means show that small objects are more deformed in all subpopulations (plot (a)). Regions A, B, and C are defined in Sheppard & Jewitt (2004) and described in Section 3. Most TNOs are in region C, and only a handful of them have an amplitude larger than 0.9 mag (plot (c)). For clarity, error bars are not plotted.

---

[14] The lightcurve of 2003 YS_{179} is considered tentative, while the lightcurve of Praamzius is secured (Kecskeméthy et al. 2023).

is the deviation between the cumulative distribution of the two samples, and a probability (Pr) between 0 and 1. If the two samples are not different from each other, the probability will be 1. We use the cold classical TNO measurements reported in Thirouin & Sheppard (2019a) as the main reference population, as the cold classical TNOs are believed to be the most primordial bodies in the solar system. Amplitudes of the 3:2 and cold classical TNOs are significantly different with $D = 0.41$ and $\mathrm{Pr} = 0.06$; similarly, $D = 0.43$ and $\mathrm{Pr} = 0.29$ for the 2:1 compared to the cold classicals. Therefore, we can consider that the 3:2 and 2:1 are not from the cold classicals. But $D = 0.18/0.36$ and $\mathrm{Pr} = 1/0.51$ for the 5:3/7:4 suggest that both resonances can be linked to the cold classical population. By comparing the resonances, we note that the 3:2 and 2:1 are similar, with $D = 0.29$ and $\mathrm{Pr} = 0.75$. However, the 3:2 and 2:1 are different from the 7:4 with $D = 0.68/0.67$ and $\mathrm{Pr} = 0.01/0.08$, respectively. By comparing the 5:3 with the 3:2 and 2:1 resonant TNOs, there is $D = 0.41/0.27$ and $\mathrm{Pr} = 0.40/0.97$.

A trans-Neptunian spin barrier at ∼4 hr has been inferred by Thirouin et al. (2010), and since then, no TNO rotating faster than this limit has been found. In this work, the fastest rotator is the 3:2 resonant (455502) 2003 UZ_{413} with a period of 4.13 ± 0.05 hr, while the slowest is the cold classical (385437) 2003 GH_{55} rotating in 210.526 ± 3.693 hr (Perna et al. 2009; Kecskeméthy et al. 2023). This time, we use the rotational periods to run some 2D K-S tests between the samples. Based on periods, the 7:4 and cold classicals are likely from the same population as $D = 0.20$ and $\mathrm{Pr} = 0.99$. Surprisingly, the 2:1 and cold classicals have $D = 0.22$ and $\mathrm{Pr} = 0.97$, suggesting that they are similar, but the 5:3 and cold classicals are less similar, with $D = 0.25$ and $\mathrm{Pr} = 0.94$. The 2D K-S test confirms that the 5:3 and 7:4 are likely from the same population ($D = 0.33$, $\mathrm{Pr} = 0.85$), whereas the 5:3 and 3:2 are from different ones ($D = 0.55$, $\mathrm{Pr} = 0.11$).

Based on the description in Section 3, the three regions to distinguish the lightcurve cause(s) are plotted in Figure 15. Only resonant and cold classicals with complete lightcurves are considered. Most of the small bodies are in region C, and only a handful of them are in regions B and A. Due to the expected low lightcurve amplitude in region A, we are probably facing an observational bias, as low-variability objects require a lot of telescope time and tend to not be reported in the literature. Region B is also scarce in objects showing that these TNOs tend to rotate slowly. Only six objects have $\Delta m \geqslant 0.9$ mag: 2001 QG_{298} (Sheppard & Jewitt 2004), 2013 FR_{28} (this work), 2003 YS_{179} and 2012 BX_{85} (Kecskeméthy et al. 2023), the satellite of 2003 QY_{90} (Kern & Elliot 2006), and 2003 BF_{91} (Trilling & Bernstein 2006). In this section, we expressed some concerns about 2003 YS_{179} and 2012 BX_{85}. Kern & Elliot (2006) published the lightcurves of 2003 QY_{90} (primary, secondary, and combined lightcurves) using six data points. The secondary's lightcurve is too sparse to detect a V or U shape, and the amplitude is highly uncertain at 0.90 ± 0.36 mag. The cold classical 2003 BF_{91} is a very small object ($H = 11.7$ mag) detected with the HST. Trilling & Bernstein (2006) found a lightcurve amplitude of 1.09 ± 0.25 mag without U/V shapes, but their data set is very noisy, and they do not discuss if this object can be a contact binary. Thirouin & Sheppard (2019a) already discussed this issue regarding this data set, and we follow their conclusions. In summary, only 2001 QG_{298} and 2013 FR_{28} are most likely contact binaries (Sheppard & Jewitt 2004; Lacerda 2011).

6. Conclusion

Our lightcurve study of the TNOs trapped in the 5:3 and 7:4 mean-motion resonances with Neptune produces the following conclusions.

1. We report several elongated objects with asymmetric lightcurves that we can interpret as albedo spot(s) on the object's surface: 2001 QF_{331}, 2014 DK_{143}, and 2015 FP_{345}.
2. With a full lightcurve amplitude of 0.94 ± 0.02 mag, 2013 FR_{28} in the 7:4 resonance is the small body in the trans-Neptunian belt with the second-largest lightcurve amplitude detected with ground-based observations after (139775) 2001 QG_{298}, whose variability was 1.14 ± 0.04 mag in 2002–2003 (Sheppard & Jewitt 2004). Modeling suggests that 2013 FR_{28} has a mass ratio of approximately 1 for a density of around 1 g cm^{-3}, and that the primary–secondary separation is less than 200 km.
3. Aside from the most likely contact binary 2013 FR_{28}, we also find four likely contact binaries—2003 SP_{317}, 2004 SC_{60}, 2006 CJ_{69}, and 2013 BN_{82}—and three (highly) elongated TNOs—2001 QF_{331}, 2003 YW_{179}, and 2015 FP_{345}. All elongated and contact binaries are at low inclinations, $i \leqslant 10°$, except for 2006 CJ_{69}, and have an ultrared surface, except for Manwë–Thorondor and 2004 SC_{60}. We flag 1999 HT_{11}, 2004 VE_{131}, and 2014 OL_{394} as potential contact binaries necessitating more data for an in-depth study.
4. Using the literature and our survey, we infer that there are 10%–50% of (nearly) equal-sized contact binaries in the 5:3 and 20%–55% in the 7:4 resonances. The fraction of contact binaries is compatible with the one predicted by Nesvorný & Vokrouhlický (2019), and it appears to be higher than the cold classical fraction (Thirouin & Sheppard 2019a).
5. Contact binary rotational periods span a large range of values from about 6 to nearly 60 hr, but most of them have a periodicity of 10–15 hr. Using the lightcurves of all known contact binaries across the trans-Neptunian belt, we report that their rotational frequency distribution follows a Maxwellian distribution. The mean rotational period of the contact binaries based on a Maxwellian distribution fit is 11.21 ± 1.76 hr, which is slow compared to the rest of the trans-Neptunian belt. One result from Brunini (2023) is the rotational period distribution of the 3:2 resonant contact binaries, and despite the fact that this distribution is only for one subpopulation, the complete contact binary population seems to follow the Brunini (2023) distribution.
6. Overall, the rotational properties of the 5:3 and 7:4 resonants are similar to the ones of the dynamically cold classicals because (1) by fitting a Maxwellian fit to the rotational frequency distribution, the mean period of our sample and the literature is 10.67 ± 1.93 hr, which infers that these resonants are slow rotators, as the dynamically cold classicals are (Thirouin & Sheppard 2019a); (2) the high average lightcurve amplitude at 0.47 mag suggests that the resonants are also far from spheroidal objects; and (3) there is a very strong correlation between lightcurve amplitude and rotational period, which is also

in the cold classical belt but not reported in other subpopulations.

7. 2D K-S tests suggest that the 5:3 and 7:4 are drawn from the same parent population, which is likely the cold classical one. Based on the lightcurve amplitude, the 5:3 is related to the cold classical, but the 7:4 is closely related to the cold classical based on rotational periods. The amplitude and period of the 3:2 TNOs are inconsistent with an origin as cold classicals. The amplitude of the 2:1 is similar to the 3:2 and inconsistent with cold classicals, but the periods of the 2:1 are similar to the cold classicals.
8. Based on surface colors (Sheppard 2012), binary fractions (Noll et al. 2020), and rotational properties (this work), we strengthen the case that the cold classicals and several resonant TNOs are linked. By studying different subpopulations, we can provide a global picture of the trans-Neptunian belt, as well as find links between subpopulations, but also probe Neptune's migration and capture mechanisms (Murray-Clay & Schlichting 2011).
9. By discovering and characterizing close/contact binaries across the trans-Neptunian belt, we aim to first of all increase the number of them but also probe their characteristics in several subpopulations, as well as provide inputs for formation and evolution models, which is still an open question for these systems (Brunini 2023).

Acknowledgments

This paper is dedicated to Josiane and Edmond Bouchand. This paper includes data gathered with the 6.5 m Magellan-Baade Telescope located at Las Campanas Observatory, Chile. This research is based on data obtained at the Lowell Discovery Telescope (LDT). Lowell Observatory is a private, nonprofit institution dedicated to astrophysical research and public appreciation of astronomy and operates the LDT in partnership with Boston University, the University of Maryland, the University of Toledo, Northern Arizona University, and Yale University. Partial support of the LDT was provided by Discovery Communications. LMI was built by Lowell Observatory using funds from the National Science Foundation (AST-1005313). We are grateful to the Magellan and LDT staffs. The authors thank William M. Grundy for sharing the list of 7:4 and 5:3 resonant TNOs observed with the Hubble Space Telescope. A.T. would like to thank her observing assistants, Thierry, Annick, and Zorro, for keeping her fed, highly (borderline over-) caffeinated, and awake/entertained while observing remotely from France with a 9 hr time difference. The authors thank two reviewers for their careful reading of this paper.

The authors acknowledge support from the National Science Foundation with grant 1734484 awarded to the "Comprehensive Study of the Most Pristine Objects Known in the Outer Solar System" and grant 2109207 awarded to the "Resonant Contact Binaries in the Trans-Neptunian Belt."

Facilities: LDT, Magellan:Baade.

Appendix A
Appendix Figures

The incomplete lightcurves discussed in this paper are reported in Figures 16 and 17.

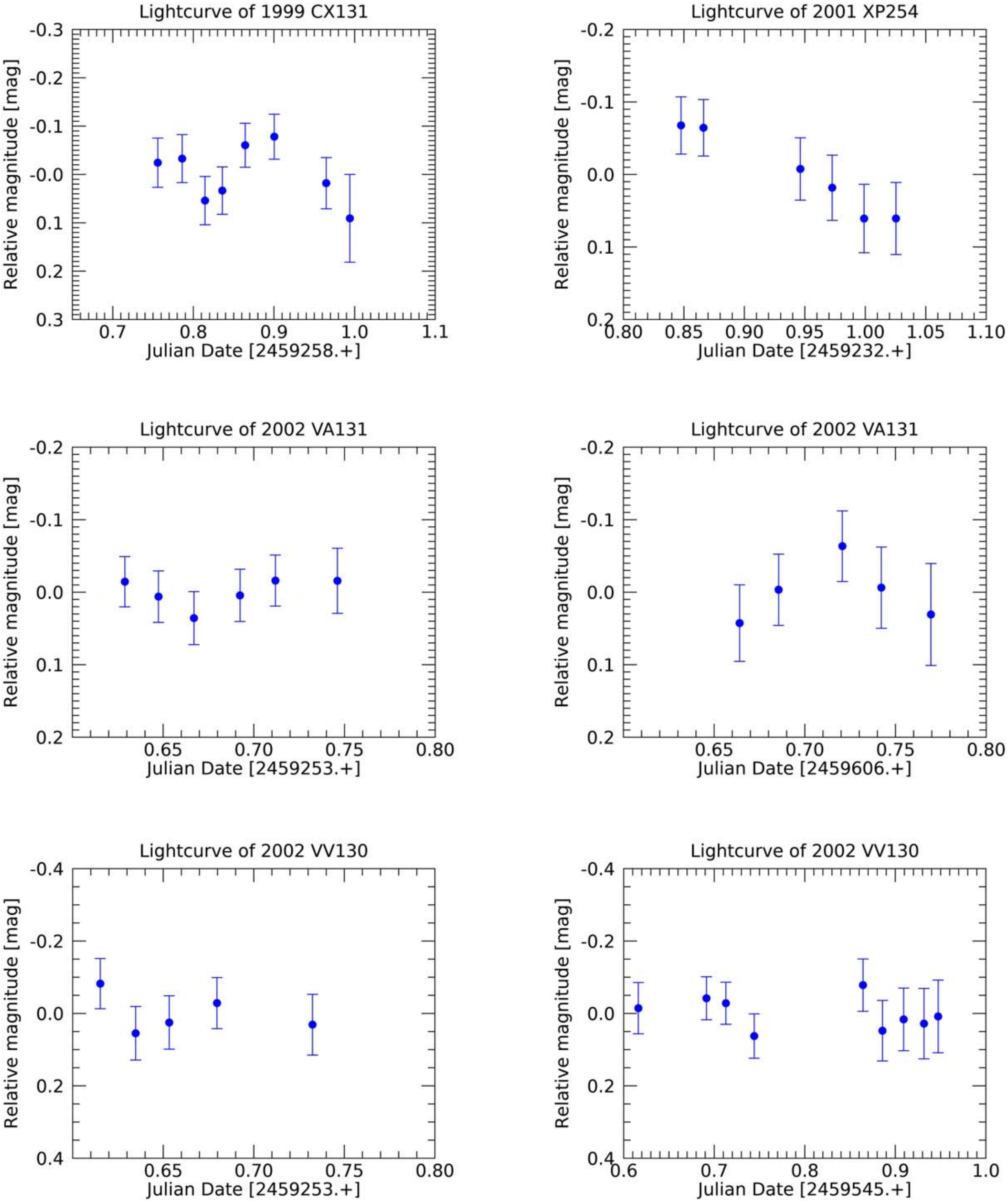
Lightcurve of 1999 CX131

Lightcurve of 2001 XP254

Lightcurve of 2002 VA131

Lightcurve of 2002 VA131

Lightcurve of 2002 VV130

Lightcurve of 2002 VV130

Figure 16. Objects in the 5:3 mean-motion resonance with Neptune.

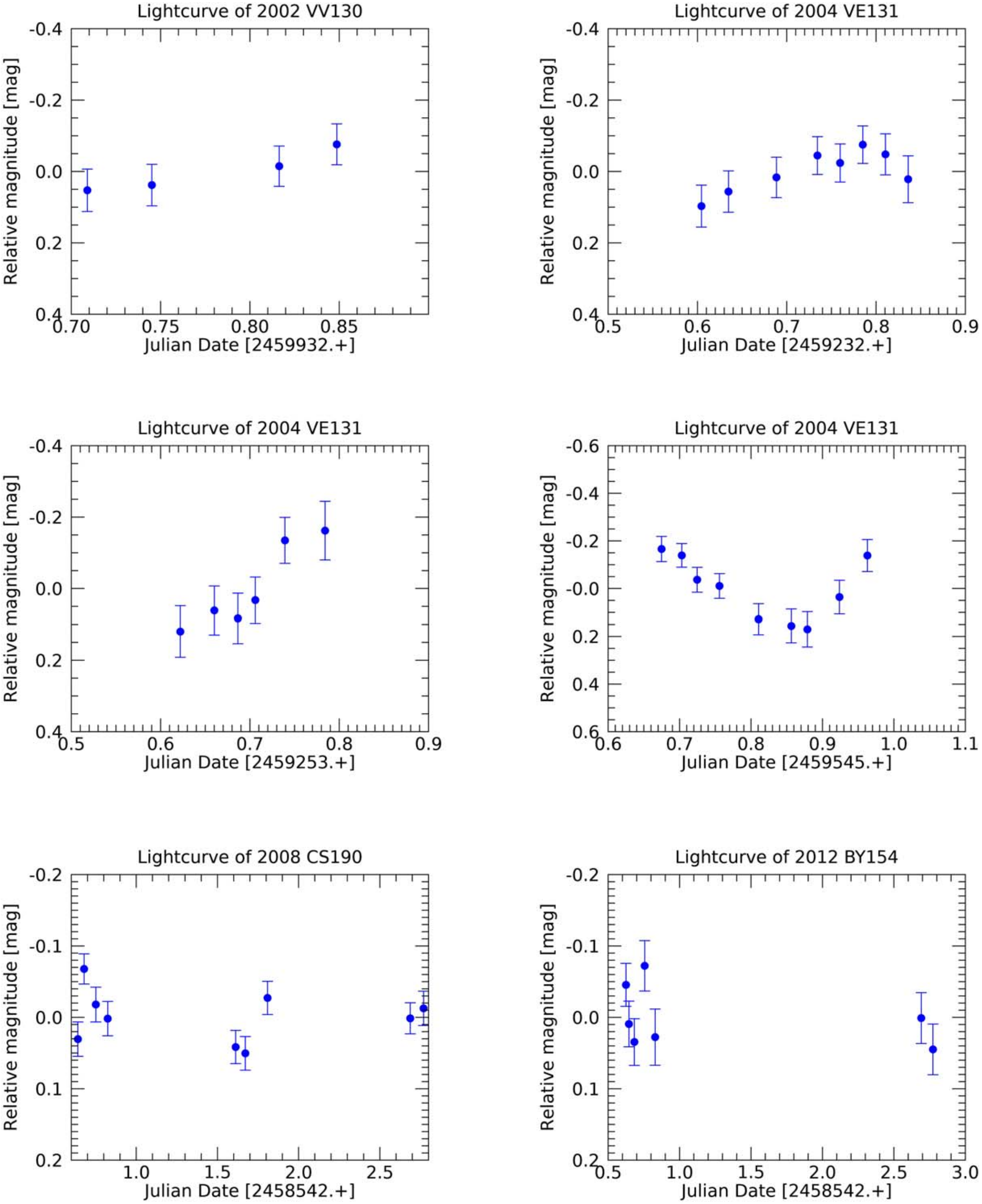

Figure 16. (Continued.)

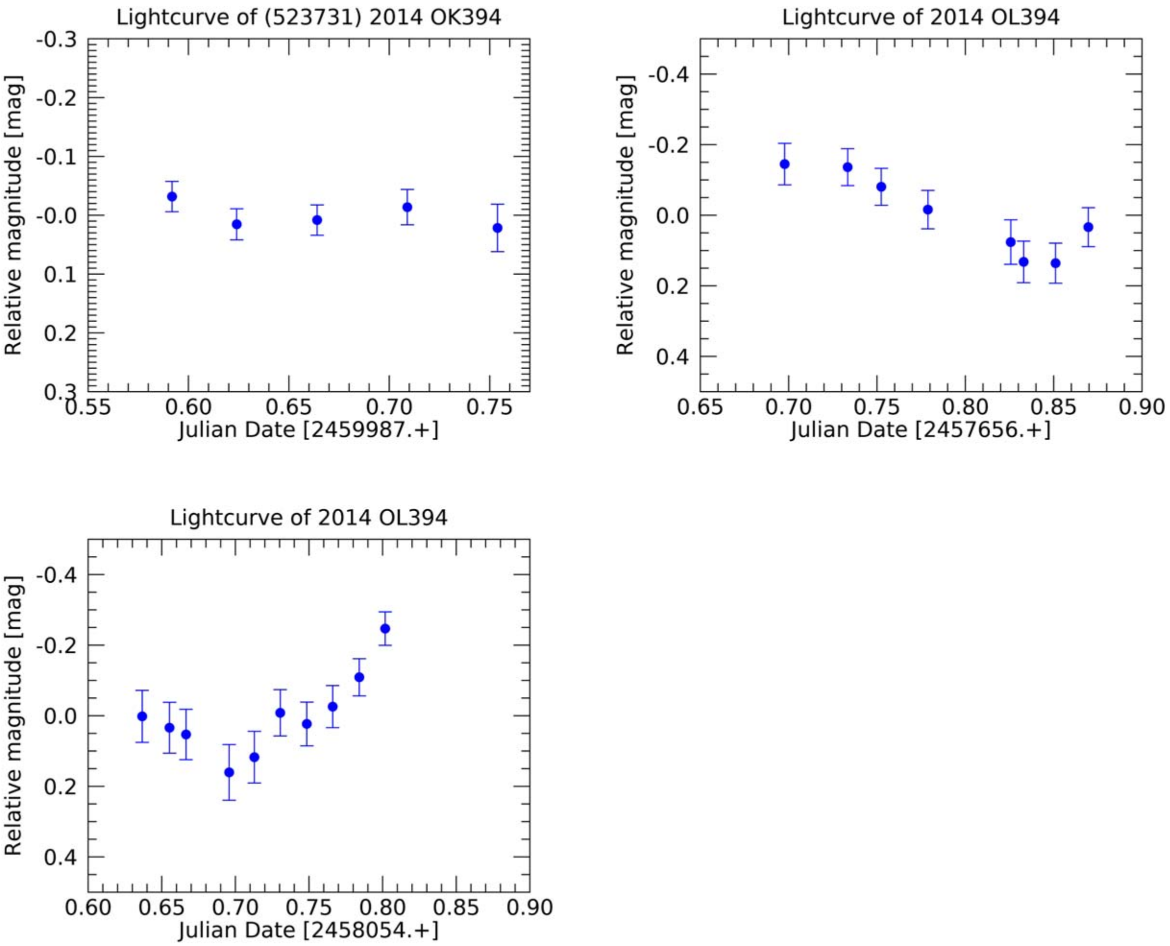

Figure 16. (Continued.)

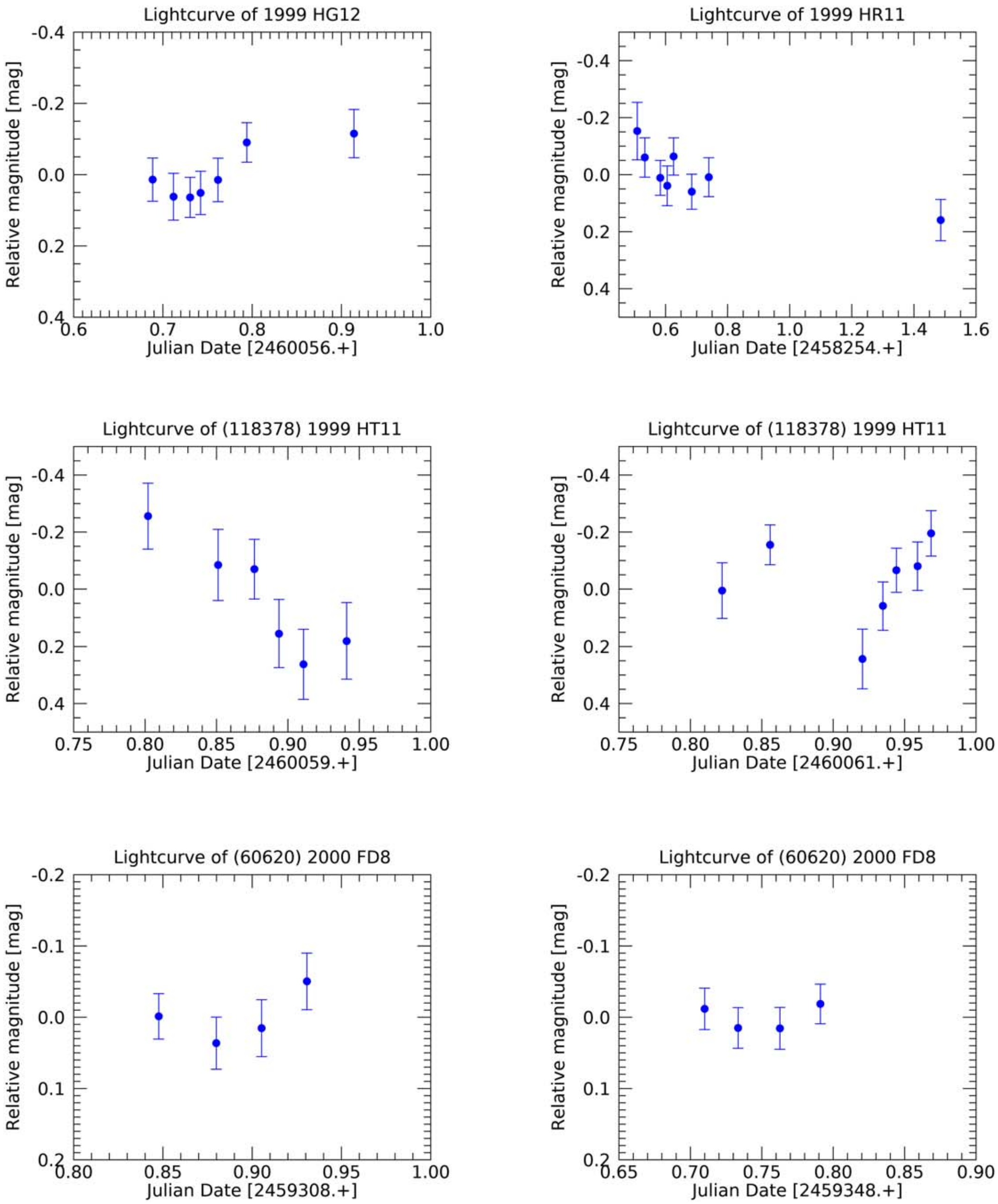

Figure 17. Objects in the 7:4 mean-motion resonance with Neptune.

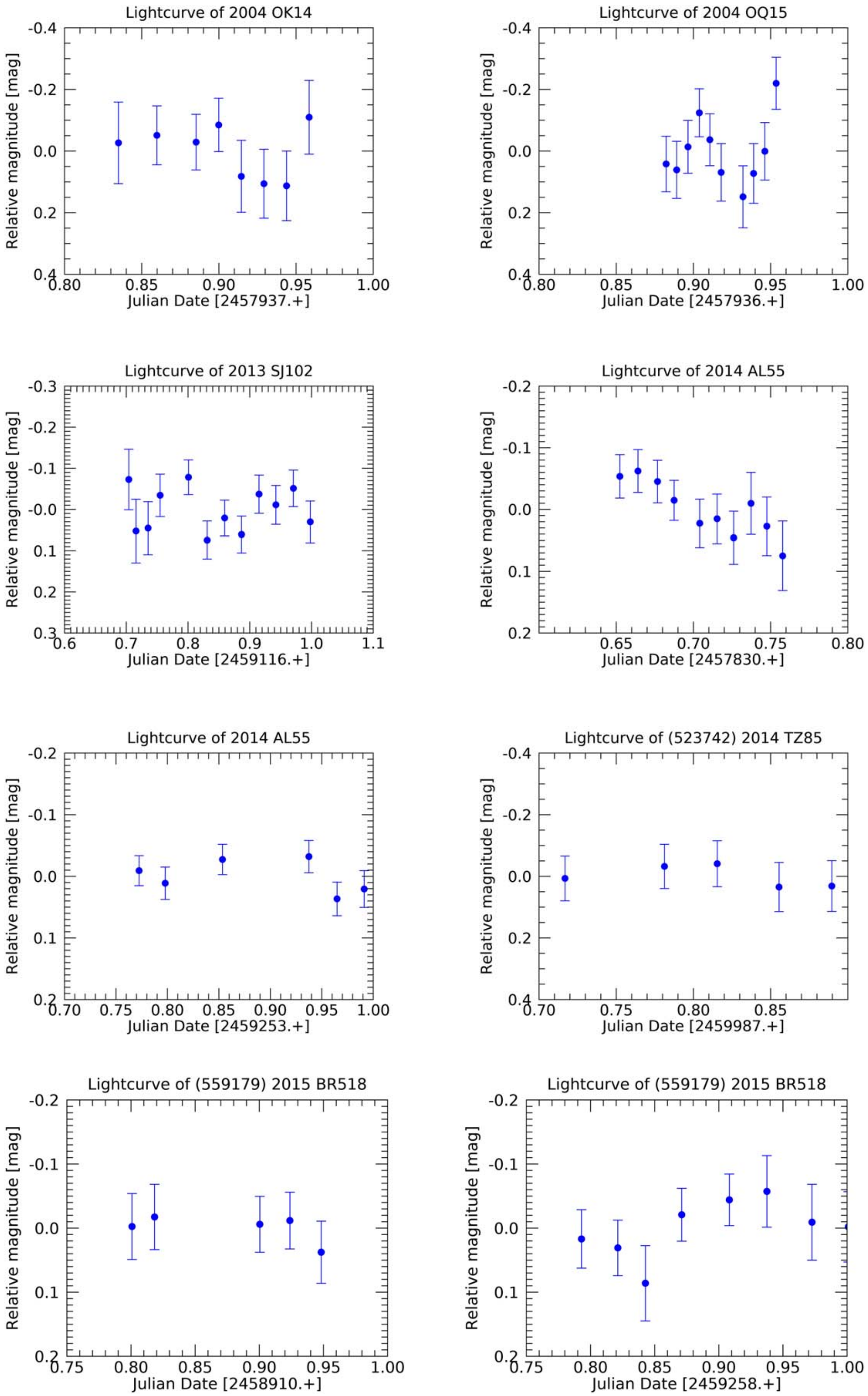
Lightcurve of 2004 OK14
Relative magnitude [mag]
-0.4
-0.2
0.0
0.2
0.4
0.80
0.85
0.90
0.95
1.00
Julian Date [2457937.+]
Lightcurve of 2004 OQ15
Relative magnitude [mag]
-0.4
-0.2
0.0
0.2
0.4
0.80
0.85
0.90
0.95
1.00
Julian Date [2457936.+]
Lightcurve of 2013 SJ102
Relative magnitude [mag]
-0.3
-0.2
-0.1
-0.0
0.1
0.2
0.3
0.6
0.7
0.8
0.9
1.0
1.1
Julian Date [2459116.+]
Lightcurve of 2014 AL55
Relative magnitude [mag]
-0.2
-0.1
0.0
0.1
0.2
0.65
0.70
0.75
0.80
Julian Date [2457830.+]
Lightcurve of 2014 AL55
Relative magnitude [mag]
-0.2
-0.1
0.0
0.1
0.2
0.70
0.75
0.80
0.85
0.90
0.95
1.00
Julian Date [2459253.+]
Lightcurve of (523742) 2014 TZ85
Relative magnitude [mag]
-0.4
-0.2
0.0
0.2
0.4
0.70
0.75
0.80
0.85
Julian Date [2459987.+]
Lightcurve of (559179) 2015 BR518
Relative magnitude [mag]
-0.2
-0.1
0.0
0.1
0.2
0.75
0.80
0.85
0.90
0.95
1.00
Julian Date [2458910.+]
Lightcurve of (559179) 2015 BR518
Relative magnitude [mag]
-0.2
-0.1
0.0
0.1
0.2
0.75
0.80
0.85
0.90
0.95
1.00
Julian Date [2459258.+]

(Continued.)

Appendix B

The photometry of all targets observed in this paper are listed in Table 7. No light-time correction is applied.

Table 7
Photometry of All Targets

Object	Julian Date	Relative Magnitude (mag)	Error (mag)
1999 CX_{131}			
	2459258.75547	−0.02	0.05
	2459258.78617	−0.03	0.05
	2459258.81438	0.05	0.05
	2459258.83591	0.03	0.05
	2459258.86422	−0.06	0.05
	2459258.90054	−0.08	0.05
	2459258.96507	0.02	0.05
	2459258.99426	0.09	0.09

(This table is available in its entirety in machine-readable form.)

ORCID iDs

Audrey Thirouin https://orcid.org/0000-0002-1506-4248
Scott S. Sheppard https://orcid.org/0000-0003-3145-8682

References

Alexandersen, M., Benecchi, S. D., Chen, Y.-T., et al. 2019, ApJS, 244, 19
Bannister, M. T., Gladman, B. J., Kavelaars, J. J., et al. 2018, ApJS, 236, 18
Benecchi, S. D., & Sheppard, S. S. 2013, AJ, 145, 124
Binzel, R. P., Farinella, P., Zappala, V., & Cellino, A. 1989, in Asteroids II, ed. R. P. Binzel, T. Gehrels, & M. S. Matthews (Tucson, AZ: Univ. Arizona Press), 416
Brunini, A. 2023, MNRAS, 524, L45
Buie, M. W., Porter, S. B., Tamblyn, P., et al. 2020, AJ, 159, 130
Chandrasekhar, S. 1987, Ellipsoidal Figures of Equilibrium (New York: Dover)
Degewij, J., Tedesco, E. F., & Zellner, B. 1979, Icar, 40, 364
Dias-Oliveira, A., Sicardy, B., Ortiz, J. L., et al. 2017, AJ, 154, 22
Elliot, J. L., Kern, S. D., Clancy, K. B., et al. 2005, AJ, 129, 1117
Gladman, B., Lawler, S. M., Petit, J. M., et al. 2012, AJ, 144, 23
Gladman, B., Marsden, B. G., & Vanlaerhoven, C. 2008, in The Solar System Beyond Neptune, ed. M. A. Barucci et al. (Tucson, AZ: Univ. Arizona Press), 43
Grundy, W. M., Benecchi, S. D., Porter, S. B., & Noll, K. S. 2014, Icar, 237, 1
Isobe, T., Feigelson, E. D., & Nelson, P. I. 1986, ApJ, 306, 490
Jeans, J. H. 1919, Problems of Cosmogony and Stellar Dynamics (Cambridge: Cambridge Univ. Press)
Jewitt, D. C., & Sheppard, S. S. 2002, AJ, 123, 2110
Kecskeméthy, V., Kiss, C., Szakáts, R., et al. 2023, ApJS, 264, 18
Kern, S. D. 2006, PhD thesis, MIT
Kern, S. D., & Elliot, J. L. 2006, Icar, 183, 179
Lacerda, P. 2011, AJ, 142, 90
Lacerda, P., Fornasier, S., Lellouch, E., et al. 2014a, ApJL, 793, L2
Lacerda, P., Jewitt, D., & Peixinho, N. 2008, AJ, 135, 1749
Lacerda, P., & Jewitt, D. C. 2007, AJ, 133, 1393
Lacerda, P., McNeill, A., & Peixinho, N. 2014b, MNRAS, 437, 3824
Lawler, S. M., Pike, R. E., Kaib, N., et al. 2019, AJ, 157, 253
Leiva, R., Buie, M. W., Keller, J. M., et al. 2020, PSJ, 1, 48
Leiva, R., Ortiz, J., Gomez-Limon, J., et al. 2023, in Asteroids, Comets, Meteors Conf., 2851
Leone, G., Paolicchi, P., Farinella, P., & Zappala, V. 1984, A&A, 140, 265
Levison, H. F., Morbidelli, A., Van Laerhoven, C., Gomes, R., & Tsiganis, K. 2008, Icar, 196, 258
Lomb, N. R. 1976, Ap&SS, 39, 447
Lykawka, P. S., & Mukai, T. 2005, P&SS, 53, 1175
Malhotra, R. 1995, AJ, 110, 420
Murray-Clay, R. A., & Schlichting, H. E. 2011, ApJ, 730, 132
Nesvorný, D. 2021, ApJL, 908, L47
Nesvorný, D., & Vokrouhlický, D. 2019, Icar, 331, 49
Nesvorný, D., Vokrouhlický, D., & Fraser, W. C. 2022, AJ, 163, 137
Noll, K., Grundy, W. M., Nesvorný, D., & Thirouin, A. 2020, in The Trans-Neptunian Solar System, ed. D. Prialnik, M. A. Barucci, & L. Young (Amsterdam: Elsevier), 201
Noll, K. S., Grundy, W. M., Stephens, D. C., & Levison, H. F. 2006, IAUC, 8745, 1
Ortiz, J. L., Gutiérrez, P. J., Santos-Sanz, P., Casanova, V., & Sota, A. 2006, A&A, 447, 1131
Pál, A., Szabó, R., Szabó, G. M., et al. 2015, ApJL, 804, L45
Peixinho, N., Delsanti, A., & Doressoundiram, A. 2015, A&A, 577, A35
Perna, D., Dotto, E., Barucci, M. A., et al. 2009, A&A, 508, 451
Pike, R. E., Fraser, W. C., Schwamb, M. E., et al. 2017, AJ, 154, 101
Pike, R. E., Fraser, W. C., Volk, K., et al. 2023, PSJ, 4, 200
Pirani, S., Johansen, A., & Mustill, A. J. 2021, A&A, 650, A161
Press, W. H., Teukolsky, S. A., Vetterling, W. T., & Flannery, B. P. 1992, Numerical Recipes in FORTRAN. The Art of Scientific Computing (2nd ed.; Cambridge: Cambridge Univ. Press)
Rabinowitz, D. L., Benecchi, S. D., Grundy, W. M., Verbiscer, A. J., & Thirouin, A. 2020, AJ, 159, 27
Sheppard, S. S. 2004, PhD thesis, Univ. Hawaii, Manoa
Sheppard, S. S. 2007, AJ, 134, 787
Sheppard, S. S. 2012, AJ, 144, 169
Sheppard, S. S., & Jewitt, D. 2004, AJ, 127, 3023
Sheppard, S. S., Lacerda, P., & Ortiz, J. L. 2008, in The Solar System Beyond Neptune, ed. M. A. Barucci et al. (Tucson, AZ: Univ. Arizona Press), 129
Spearman, C. 1904, The American Journal of Psychology, 15, 72
Thirouin, A. 2013, PhD thesis, Univ. Granada, Spain
Thirouin, A., Noll, K. S., Ortiz, J. L., & Morales, N. 2014, A&A, 569, A3
Thirouin, A., Ortiz, J. L., Duffard, R., et al. 2010, A&A, 522, A93
Thirouin, A., & Sheppard, S. S. 2017, AJ, 154, 241
Thirouin, A., & Sheppard, S. S. 2018, AJ, 155, 248
Thirouin, A., & Sheppard, S. S. 2019a, AJ, 157, 228
Thirouin, A., & Sheppard, S. S. 2019b, AJ, 158, 53
Thirouin, A., & Sheppard, S. S. 2022, PSJ, 3, 178
Thirouin, A., Sheppard, S. S., Noll, K. S., et al. 2016, AJ, 151, 148
Thirouin, A., Sheppard, S. S., & Noll, K. S. 2017, ApJ, 844, 135
Trilling, D. E., & Bernstein, G. M. 2006, AJ, 131, 1149
Volk, K., & Malhotra, R. 2011, ApJ, 736, 11
Volk, K., & Malhotra, R. 2019, AJ, 158, 64
Weidenschilling, S. J. 1980, Icar, 44, 807